Advances in Water Resources 216 (2026) 105399

Contents lists available at ScienceDirect

Advances in Water Resources

journal homepage: www.elsevier.com/locate/advwatres

Plane gravity currents in heterogeneous porous media

Sepideh Majdabadi Farahani [a], Patricio Hernández-Parra [b], Bruno Rossi [a], Vittorio Di Federico [a],*, J. Jaime Gómez-Hernández [b]

[a] Dipartimento di Ingegneria Civile, Chimica, Ambientale e dei Materiali, Alma Mater Studiorum Università di Bologna, Viale Risorgimento, 2, Bologna, 40136, Italy
[b] Institute for Water and Environmental Engineering, Universitat Politècnica de València, Camino de Vera, s/n, Valencia, 46022, Spain

ARTICLE INFO

Keywords:
Fluid dynamics
Gravity currents
Heterogeneity
Numerical simulations
Porous media
Uncertainty quantification

ABSTRACT

Gravity currents (GCs) in porous media are strongly influenced by the spatial variability of hydraulic conductivity, yet most modeling efforts assume homogeneous conditions. In this work, we develop and validate a MODFLOW–NWT numerical model capable of simulating Newtonian gravity-current propagation in both homogeneous and heterogeneous porous media. The model is first benchmarked against classical similarity solutions, showing excellent agreement as the current evolves in time.

We then investigate the influence of heterogeneity by generating ensembles of Gaussian and non-Gaussian hydraulic-conductivity fields with varying $\log_{10} K$ variance and for different anisotropy ratios. For each scenario, 100 realizations are simulated to quantify the effects of spatial variability on GC behavior. Results demonstrate that heterogeneity significantly alters the propagation dynamics, causing individual fronts to diverge from the homogeneous prediction and increasing uncertainty over time. On average, both Gaussian and non-Gaussian heterogeneity yield faster front advancement than the homogeneous case.

Probability maps reveal widening uncertainty intervals with increasing variance and anisotropy ratio, with Gaussian fields producing more stretched profiles than their non-Gaussian counterparts. Because non-Gaussian fields more closely reflect geological facies structures, they provide a more realistic basis for assessing prediction errors. These findings underscore the importance of incorporating geological heterogeneity into GC modeling, particularly for applications such as aquifer remediation and CO_2 sequestration.

1. Introduction

Gravity Currents (GCs), or density-driven flows, are predominantly horizontal motions generated by a density contrast between the intruding fluid and ambient fluids. In porous media, such currents occur in both natural and engineered systems, including seawater intrusion (Lennon et al., 1987), oil well drilling (Dussan and Auzerais, 1993), geothermal energy extraction (Woods, 1999), geological carbon sequestration (Neufeld and Huppert, 2009) and contaminant transport in the subsurface (Schneider et al., 2015).

Classical GC theory assumes Darcy flow in a homogeneous porous medium. Mixing between fluids and viscous fingering caused by capillary effects are often neglected (Huppert, 1982), leading to the idealization of a sharp interface with a characteristic nose shape at late times. Under lubrication theory assumptions, the current is considered long and thin, vertical motions are negligible and the pressure distribution is hydrostatic (Huppert and Woods, 1995; Di Federico et al., 2012).

The foundational work by Huppert and Woods (1995) established a mathematical model for the propagation of two-dimensional unconfined GCs in porous media over horizontal and inclined and boundaries. Using similarity solutions, they predicted current extension and validated their model experimentally. Subsequent studies extended this framework to more complex configurations, including GCs in porous rocks (Woods, 1998), layered formations (Woods and Mason, 2000), axisymmetric flows (Lyle et al., 2005), and systems with sinks or permeable substrates (Mathunjwa and Hogg, 2007; Zheng et al., 2013). Additional studies investigated the influence of non-Newtonian rheology (Di Federico et al., 2012; Longo et al., 2015) and surface topography (Pegler et al., 2013; Maggi et al., 2023).

Despite these advances, a key simplifying assumption persists: treating the porous medium as homogeneous. In reality, geological formations are highly heterogeneous due to complex depositional processes (Benham et al., 2021), resulting in values of hydraulic conductivity that can span several orders of magnitude at the sub-meter scale (Savoy et al., 2017). A common form of large-scale heterogeneity is the presence of thin, approximately horizontal, low-permeability layers (Hewitt et al., 2020). Although several studies have examined GCs in such settings, these investigations remain limited and typically rely on simplified representations.

* Corresponding author.
E-mail address: vittorio.difederico@unibo.it (V. Di Federico).

https://doi.org/10.1016/j.advwatres.2026.105399
Received 17 December 2025; Received in revised form 17 June 2026; Accepted 27 June 2026
Available online 3 July 2026

Fig. 1. Representative example of subsurface heterogeneity from the Hunter Valley coal mine, Australia (image courtesy of Hassan Abbas) (Michigan State University, 2005).

For example, Anderson et al. (2003) analyzed slumping GCs in homogeneous and periodically heterogeneous media using homogenization theory. Ciriello et al. (2013) explored the influence of anisotropic permeability variations by imposing a deterministic, monotonic power-law distribution, enabling them to generalize classical closed-form solutions while outlining conditions for model validity. Similarly, Farcas and Woods (2015) studied flow through multi-layer systems, showing that flow speed increases with depth and that, under pressurized injection, longitudinal dispersion can split tracer pulses into distinct arrivals. Sahu and Neufeld (2020) further demonstrated that increasing heterogeneity enhances interface instability and amplifies deviations from sharp-interface behavior at later times.

Experimental studies on two-layer and multi-layer systems, including Goda and Sato (2011), Huppert et al. (2013), and Sahu and Neufeld (2023), consistently show a thickened current nose and partitioning of flow across layers relative to homogeneous cases.

In the context of CO_2 sequestration, several investigations have incorporated more realistic conditions, including capillarity and mixing. For instance, Krevor et al. (2011) characterized capillary trapping in a sandstone core under reservoir conditions, while others examined CO_2 migration in heterogeneous formations (Benham et al., 2021; Alamara et al., 2025).

In groundwater contamination/remediation studies, heterogeneity is commonly considered to assess how solutes spread in the subsurface as a function of the site's lithologic configuration (Michael and Khan, 2016; Guo et al., 2019). In contrast, gravity currents developing in porous media are inherently sensitive to variations in local properties, yet the role of small- to intermediate-scale heterogeneity on their dynamics remains poorly understood. To the best of our knowledge, in the context of groundwater remediation processes driven by density contrasts, subsurface heterogeneity is often either neglected or represented only at a coarse scale (Tosco et al., 2014; Maxwell et al., 2008), potentially overlooking its impact on flow structure and mixing.

As summarized above, studies of GCs in heterogeneous porous media remain limited, and those that do exist often impose simplified or deterministic descriptions of heterogeneity (Flicos and Neufeld, 2025). However, since small-scale heterogeneity is ubiquitous in underground formations, it is essential to assess the impact of such variability on gravity current propagation. Realistic predictions require a stochastic framework capable of capturing the intrinsic variability of geological formations, making uncertainty quantification (UQ) a key component in the probabilistic characterization of GC spreading. Existing UQ approaches, however, are largely restricted to Gaussian random fields (Crevillén-García et al., 2019; Mo et al., 2019), which may inadequately represent the layered structure commonly encountered in sedimentary environment (see Fig. 1).

While a few stochastic studies have examined the influence of small-scale variability in porous-medium properties on free-surface flows (e.g., Tartakovsky and Winter (2001); Amir and Dagan (2002)) they did not specifically address gravity currents.

The present work aims to determine the impact of small-scale heterogeneity on fluid propagation in underground porous structures by introducing and validating a MODFLOW-based numerical model capable of incorporating heterogeneity in the GC flow problem. We investigate the influence of heterogeneity on the evolution of a Newtonian GC by representing the spatial variability of hydraulic conductivity as both Gaussian and non-Gaussian random fields. For each class of heterogeneity, six configurations are considered, combining two flow regimes (dam-break release and constant injection) with three levels of logarithmic variance. In all cases, the mean conductivity matches that of a reference homogeneous medium. For each configuration, 100 independent realizations are generated, producing corresponding current profiles. To quantify uncertainty, probability maps of the saturation profiles are constructed using an approach resembling the probabilistic estimation of well catchments in heterogeneous confined aquifers presented by Franzetti and Guadagnini (1996). The results are then compared to assess how different heterogeneity structures influence GC spreading relative to the homogeneous benchmark, showing that heterogeneity significantly affects the fluid propagation even in the simplest flow scenario. This methodological work may find applicability in more advanced studies, such as multiphase flow problems like in geological CO_2 sequestration or transport analyses for groundwater remediation, where the inclusion of the spatial variability of the medium parameters would considerably impact the CO_2 or contaminant spreading in the underground. This is so since, to the best of our knowledge, there are no previous studies that address the effect on such subsurface flows of a small-scale heterogeneity as the one described within the present work.

In particular, the enhanced spreading of the current induced by small-scale variability in medium properties demonstrates the importance of accounting for heterogeneity when describing and predicting subsurface flow phenomena. This conclusion is supported by the analysis of a comprehensive set of heterogeneity scenarios, encompassing

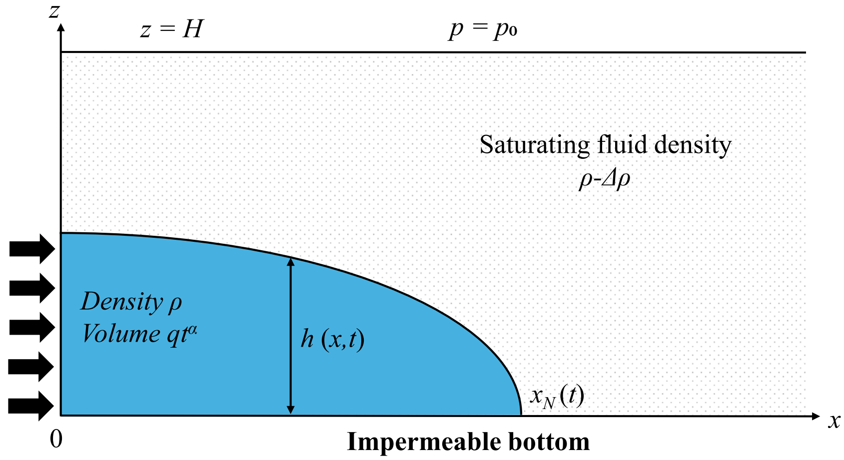

Fig. 2. Sketch of a two-dimensional gravity current intruding a saturated porous medium.

different conductivity field variances and anisotropy settings. Furthermore, the comparison between Gaussian and non-Gaussian fields provides additional insight into the importance of realistically representing subsurface formations, rather than relying solely on standard stochastic descriptions. By highlighting the role of small-scale heterogeneity, these findings contribute to the improved design and management of groundwater and subsurface engineering applications, including: (i) contamination by Dense Non-Aqueous Phase Liquid (DNAPL) or radioactive leachates, as heterogeneity controls preferential migration pathways and pooling zones; (ii) groundwater remediation, since the delivery efficiency of dense amendments depends on heterogeneity-controlled spreading; (iii) saline groundwater intrusion, as heterogeneity influences interface shape and advance rate of inland migrating plumes; (iv) brine leakage from deep storage formations, and (v) geological CO_2 storage, both in the case of near-well gravity currents during injection and post-injection spreading beneath caprocks, because heterogeneity affects plume footprint, residual trapping, and leakage risk. In such settings, inadequate representations of medium heterogeneity may lead to significant errors in predicting plume migration and spreading patterns, with consequent implications for risk assessment and economic evaluations. For example, neglecting small-scale heterogeneity may lead to an underestimation of the uncertainty associated with contaminant migration, fostering excessive confidence in remediation predictions and potentially resulting in suboptimal remediation designs and unforeseen operational costs. Other related applications are hydrogen, gas or compressed air storage, cold-water re-injection, density-driven flow in sedimentary basins, and subsurface batteries.

The paper is organized as follows. Section 2 presents the classical similarity solution of Huppert and Woods (1995). Section 3 validates the MODFLOW model for homogeneous conditions. Section 4 examines the effects of Gaussian and non-Gaussian heterogeneity. Finally, Section 5 summarizes the findings and main conclusions.

2. Theoretical framework

We consider the two-dimensional flow of a fluid intruding into a saturated porous medium, as illustrated in Fig. 2. The motion is driven by a density difference ($\Delta\rho$) between the intruding and ambient fluids. As in classical gravity current (GC) problems, the flow through the porous medium is assumed to be sufficiently slow that the inertial term in the Navier–Stokes equation can be neglected. Consequently, the momentum balance involves only buoyancy and viscous forces. For such a viscous GC, the flow regime is Darcian provided that the pore-scale Reynolds number remains below a critical threshold, a condition typically satisfied in subsurface flows except in very coarse media or near injection wells (Bear, 1972). Assuming the ambient fluid is static and that vertical velocities are negligible for a long and thin current ($h \ll L$), the pressure distribution within the current is hydrostatic (lubrication approximation) and can be written as (Huppert, 1982)

$$p = p_0 + (\rho - \Delta\rho)g\,(H - h) + \rho g\,(h - z)\,, \tag{1}$$

where p_0 is the atmospheric pressure, ρ is the density of the current, g is the gravitational acceleration, H is the thickness of the ambient fluid, and $h(x,t)$ is the local height of the current. Applying Darcy's law, the velocity and pressure in the porous medium are related through

$$u = -\frac{k(\phi)}{\mu}(\nabla p - \rho\mathbf{g}), \tag{2}$$

where k is the intrinsic permeability of the medium $\left[L^2\right]$, ϕ is the porosity of the medium, μ is the dynamic viscosity of the intruding fluid $[MT^{-1}L^{-1}]$ and $\mathbf{g} \equiv (0, 0, -g)$ is the gravity vector.

A common simplification in calculating the Darcy velocity is to assume that the porous medium has a homogeneous permeability (Huppert and Woods, 1995; Di Federico et al., 2012), an assumption that will be adopted throughout this Section.

To predict the pattern of current propagation, it is essential to determine its height $h(x,t)$. This quantity is governed by the local mass balance equation:

$$\phi\frac{\partial h}{\partial t} = -\frac{\partial}{\partial x}\left(\int_0^h u\,dz\right), \tag{3}$$

together with global mass conservation – which is equivalent to prescribing a flux boundary condition at the origin – and the boundary condition at the nose. These two conditions are given by:

$$\phi\int_0^{x_N(t)} h(x,t)\,\mathrm{d}x = qt^\alpha, \quad h(x_N(t),t) = 0, \tag{4}$$

where ϕ is the porosity of the medium, x_N denotes the maximum horizontal extent of the GC (i.e., the nose of the current), and q has dimensions of $\left[L^2T^{-\alpha}\right]$. The exponent α specifies the injection regime, corresponding to a dam-break release (finite volume) for $\alpha = 0$ and to constant injection for $\alpha = 1$. Substituting Eq. (2) into Eq. (3) yields the following nonlinear PDE:

$$\frac{\partial h}{\partial t} = V\frac{\partial}{\partial x}\left(h\frac{\partial h}{\partial x}\right), \tag{5}$$

which describes the GC flow, where $V = \frac{k\Delta\rho g}{\mu\phi}$ has the dimensions of a velocity $[LT^{-1}]$. The differential problem can be rewritten in a dimensionless form by introducing the non-dimensional variables $T = t/t^*$, $x = x/x^*$, $x_N = x_N/x^*$, $H = h/x^*$, where the time, length and velocity scales are

$$t^* = \left(\frac{q}{\phi v^{*2}}\right)^{\frac{1}{2-\alpha}}, \quad v^* = V, \quad x^* = Vt^*. \tag{6}$$

Note that V can be rewritten in terms of the hydraulic conductivity $K = \frac{k\rho g}{\mu}$ ($[LT^{-1}]$) as

$$V = \frac{k\Delta\rho g}{\mu\phi} = \frac{\Delta\rho}{\rho\phi}K. \tag{7}$$

Substituting Eqs. (6) into Eqs. (3) and (4) yields

$$\frac{\partial H}{\partial T} = \frac{\partial}{\partial X}\left(H\frac{\partial H}{\partial X}\right), \tag{8}$$

$$\int_0^{X_N} H\,\mathrm{d}X = T^{\alpha}. \tag{9}$$

This dimensionless differential problem can be solved by introducing the following similarity scalings:

$$\xi = XT^{-(\alpha+1)/3}, \quad H = \xi_N^2 T^{(2\alpha-1)/3}\Phi(\zeta), \tag{10}$$

where $\zeta = \xi/\xi_N$ is the scaled similarity variable and Φ is the eigenfunction (or shape function), that describes the self-similar shape of the current (Barenblatt, 1996). Substituting Eqs. (10) into Eqs. (8) and (9) reduces the problem to a nonlinear ODE:

$$\frac{d}{d\zeta}\left[\Phi\frac{d\Phi}{d\zeta}\right] + \left(\frac{\alpha+1}{3}\right)\zeta\frac{d\Phi}{d\zeta} - \left(\frac{2\alpha-1}{3}\right)\Phi = 0, \tag{11}$$

$$\xi_N = \left[\int_0^1 \Phi\mathrm{d}\zeta\right]^{-1/3}, \tag{12}$$

together with the boundary condition at the nose, $\Phi(1) = 0$.

For the case of an instantaneous injection ($\alpha = 0$), the differential problem admits a closed-form solution given by

$$\Phi(\zeta) = \frac{1}{6}(1-\zeta^2), \quad \xi_N = 9^{\frac{1}{3}}, \tag{13}$$

and, upon returning to dimensional variables, the profile of the current becomes

$$h(x,t) = \frac{1}{6}\left(\frac{q^2}{tV}\right)^{\frac{1}{3}}\left[\left(\frac{9}{\phi}\right)^{\frac{2}{3}} - \frac{x^2}{(Vqt)^{\frac{2}{3}}}\right], \tag{14}$$

which describes the evolution of the water table under the assumption of dispersion-free flow and a quasi-steady-state regime, where the initial transient effects are neglected.

For non-zero injection rates, the differential problem (11)–(12) can only be solved numerically.

As mentioned above, this approach reflects the standard practice for analyzing GCs in homogeneous porous media. In the heterogeneous case, however, the nonlinear PDE (5) cannot be solved using available analytical methods. Therefore, a numerical strategy incorporating stochastic techniques is employed to address this problem.

Since the propagation of a GC in a porous medium filled with air is analogous to free-surface flow, FLOPY–MODFLOW was selected to simulate the current. As a first step, the model was validated by comparing its predictions with the classical similarity solution for a homogeneous medium. Subsequently, Gaussian and non-Gaussian heterogeneous fields with varying degrees of variability (mild, medium, and high variance) were generated to assess how spatial fluctuations in hydraulic conductivity influence the spreading of the gravity current.

3. Numerical model description and validation

To validate the MODFLOW numerical model, we first consider a free-surface, homogeneous, and isotropic aquifer of finite extent, represented by a two-dimensional grid in the x-z plane, with uniform discretization in both horizontal and vertical directions. The domain has a length of $L_x = 20$ m and a height of $H = 10$ m, discretized into $n_x = 200$ columns and $n_z = 100$ rows, resulting in a cell size of $\Delta x = \Delta z = 0.1$ m. The hydraulic conductivity is set to $K = 0.1$ m/day and the effective porosity is taken as $\phi = 1.0$, both assumed constant throughout the domain, thereby defining a homogeneous and isotropic medium. At the left boundary ($x = 0$), an infiltration zone is imposed with an initial water table elevation of $H = 7$ m, while at the right boundary ($x = L_x$), a drainage condition is applied towards lower elevations.

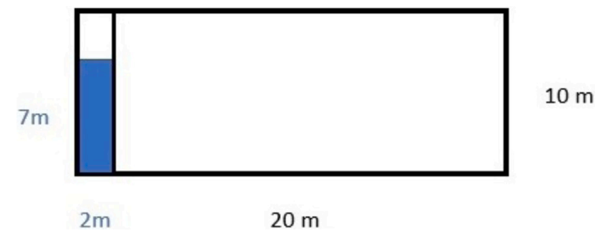

Fig. 3. Initial saturation front for the MODFLOW-NWT simulation, homogeneous medium and finite-volume release.

The numerical simulation is performed using MODFLOW. The underlying equation is

$$\frac{\partial}{\partial x}\left(K_{xx}\frac{\partial h}{\partial x}\right) + \frac{\partial}{\partial y}\left(K_{yy}\frac{\partial h}{\partial y}\right) + \frac{\partial}{\partial z}\left(K_{zz}\frac{\partial h}{\partial z}\right) + W = S_s\frac{\partial h}{\partial t} \tag{15}$$

where K_{xx}, K_{yy}, and K_{zz} are the values of hydraulic conductivity along the x, y, and z coordinate axes $[L/T]$, h is the hydraulic head $[L]$, W is a volumetric flux per unit volume representing sources and/or sinks of water $[T^{-1}]$, S_s is the specific storage of the porous material $[L^{-1}]$, and t is time $[T]$. Solving (15) with appropriate initial and boundary conditions yields the solution in terms of head h. The capability to handle cell wetting and drying allows MODFLOW to simulate the evolution of the phreatic surface that delineates the edges of the gravity current. This wetting and drying process introduces strong nonlinearity into the governing equations and, for this reason, a specialized version of MODFLOW, namely MODFLOW-NWT, is employed to ensure numerical convergence. Note also that, for the solution of the flow equation, it is necessary to provide also the porosity of the medium.

In the current exercise, cell conductivities are considered isotropic, therefore $K_{xx} = K_{yy} = K_{zz} = K$ at the cell scale, but may be heterogeneous in space. Such heterogeneity would render them anisotropic at the macroscopic scale. A convergence tolerance of 10^{-5} m is imposed in the hydraulic heads. To capture the evolution of the surface of the water table, a transient period of 50 days is simulated, divided into 50 time steps. The objective is to test the model against the analytical solution (14) for $\alpha = 0$ and the numerical similarity solution obtained from Eqs. (11) and (12) for $\alpha = 1$.

3.1. Instantaneous injection ($\alpha = 0$)

For the case $\alpha = 0$, the initial condition is prescribed such that a segment of 2 m at the left boundary is initially saturated up to a height of 0.7 H, representing the lock-release configuration for an instantaneous dam-break (see Fig. 3). The resulting finite volume per unit width is $q = 14\,\mathrm{m}^2$. This initial water volume drives the subsequent propagation of the saturation front (phreatic surface).

From Eq. (14), the initial water-table profile can be prescribed using the analytical expression

$$h(x,t) = \max\left(0, \frac{1}{6}\left(\frac{q^2}{Kt}\right)^{\frac{1}{3}}\left[9^{\frac{2}{3}} - \frac{x^2}{(Kt)^{\frac{2}{3}}}\right]\right). \tag{16}$$

This formulation simplifies the water-volume balance in the system by assuming a well-defined advancing front and neglecting mixing and hydraulic dispersion. In addition, the "max" operator ensures that the height of the water-table does not become negative, thus maintaining the physical consistency in the solution.

We observed some discrepancies between the numerical and analytical results, particularly at early times. These differences can be

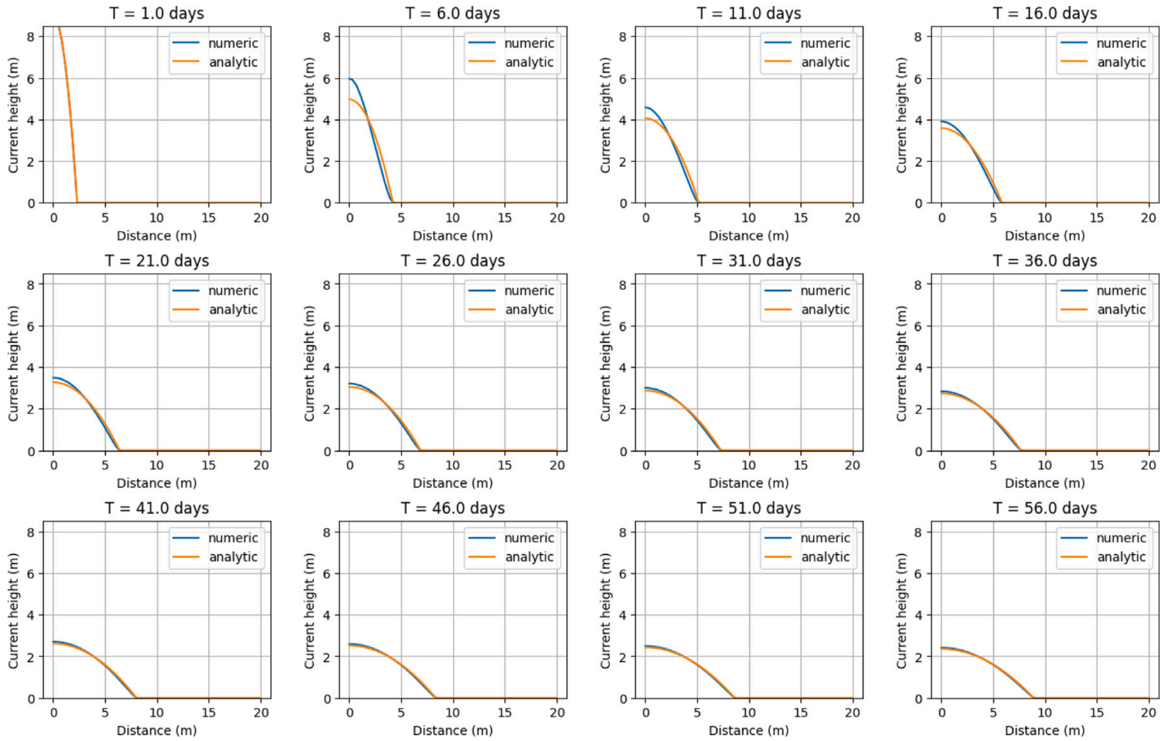

Fig. 4. Comparison between the numerical solution (MODFLOW-NWT) and the analytical solution (14) for $t_0 = 1$ day under instantaneous injection ($\alpha = 0$).

attributed to the fact that the initial conditions shown in Fig. 3 do not exactly match the analytical assumption of an instantaneous injection at $x = 0$ at time zero, corresponding to a prescribed volume per unit width q. To address this inconsistency, we modified the initial conditions of the numerical simulation by adopting the analytical solution at a finite time t_0. Specifically, the gravity current profile in a homogeneous medium, as given by the analytical solution, is used as the initial condition for the numerical model.

Fig. 4 shows a comparison between the analytical and numerical solutions when the numerical model is initialized with head distributions corresponding to $t_0 = 1$. A discrepancy is observed at early times, which progressively diminishes as the gravity current propagates.

However, when the simulation is initialized with conditions corresponding to $t_0 = 5$, as shown in Fig. 5, the agreement between the numerical and the analytical solution is nearly perfect. This confirms that the free-surface formulation implemented in MODFLOW is able to accurately reproduce gravity current migration.

3.2. Constant injection ($\alpha = 1$)

The case of constant injection rate leads to a more complex flow regime due to the nonlinear propagation of the saturation front. Although the physical domain remains unchanged, the numerical model must now account for this nonlinear behavior, which introduces a non-trivial temporal dependence in the evolution of the water table.

The same boundary conditions and simulation steps used for the $\alpha = 0$ case are retained, whereas the initial condition is now defined by a saturation front propagating within the domain, driven by a point recharge. Since for $\alpha = 1$ the ODE (11) is not amenable to a closed form solution, numerical integration is required to obtain the shape function $\Phi(\zeta)$, from which the water table profile can be written as

$$h(x,t) = \max\left(0, x^* \cdot \xi_N^2 \left(\frac{t}{t^*}\right)^{1/3} \cdot \Phi\left(\frac{x}{x_N}\right)\right), \tag{17}$$

starting from the scalings introduced in Eq. (10), where ξ_N is determined from Eq. (12). Thus, the temporal evolution of the self-similar water table profile follows a scaling law of the form $t^{1/3}$, while the nose advances as $x_N \sim t^{2/3}$. This solution characterizes the propagation of a saturation front originating from the injection zone, accounting for both the nonlinearity of the flow and its explicit temporal dependence.

When comparing the analytical results (16)–(17) with those obtained from the MODFLOW-NWT numerical simulation, we find that, regardless of the chosen value of t_0, the numerical and analytical solutions are in excellent agreement, as shown in Figs. 6 and 7.

4. Numerical solutions for heterogeneous media

Following the validation of the MODFLOW-NWT numerical scheme in Section 3, the purpose of this Section is to investigate how the current propagates when medium heterogeneity is incorporated into the model, and to quantify the impact of such heterogeneity relative to the homogeneous case.

4.1. Gaussian heterogeneity

We first represent the spatial variability of the hydraulic conductivity K using a Gaussian random field. Log-normal fields are generated by applying a Gaussian model with exponential covariance, characterized by a horizontal correlation length $\lambda_h = 4.50$ m and a vertical correlation length $\lambda_v = 0.67$ m. The mean value is fixed at $\log_{10} K = -1$, corresponding to the hydraulic conductivity previously assumed for the homogeneous case. Six configurations of the heterogeneous medium are considered by combining the two flow regimes ($\alpha = 0$ and $\alpha = 1$) with three levels of logarithmic variance of hydraulic conductivity ($\log_{10} K$): $\sigma^2 = 0.5; 1.0; 2.0$. For each configuration, 100 independent realizations are generated. A selection of these realizations is shown in Fig. 8.

The initial conditions are computed from the analytical solutions at $t = 5$ days, after which the transient flow is simulated using MODFLOW-NWT. The boundary conditions remain the same as in the homogeneous case and depend only on the specified value of α.

The temporal evolution of the water-table levels was computed for all 100 realizations.

Fig. 9 compares the current profiles in a homogeneous medium with those obtained for one heterogeneous realization. The left panel shows

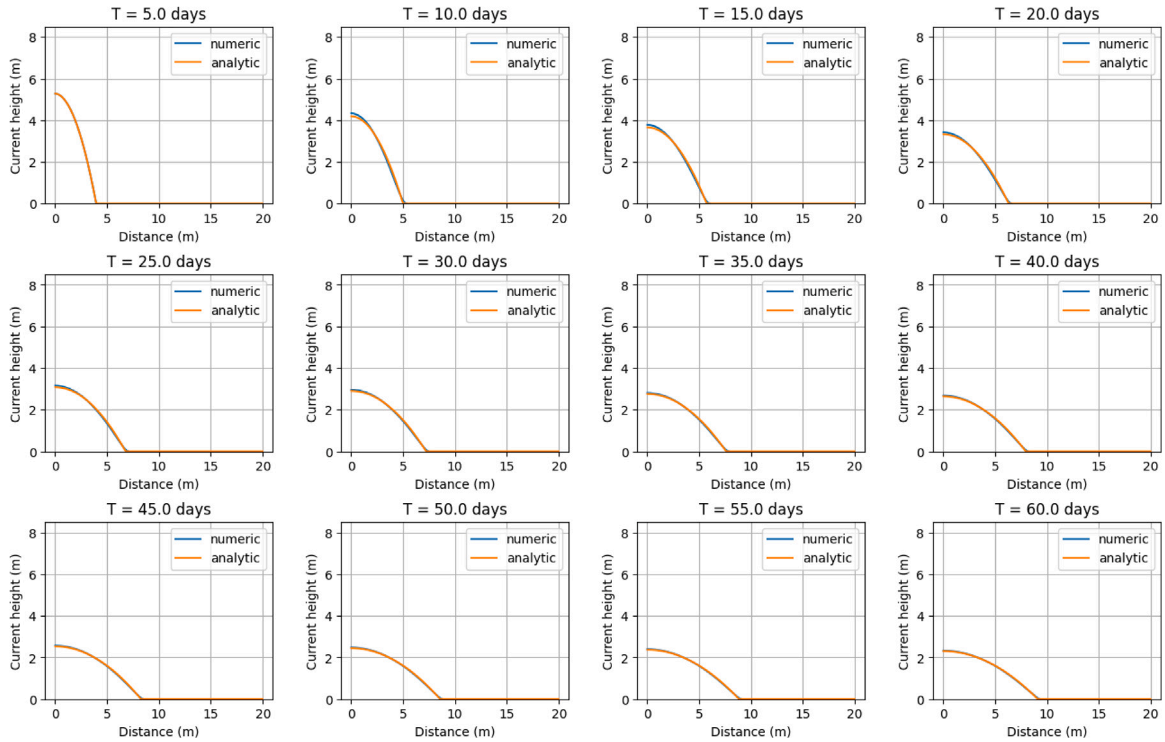

Fig. 5. Comparison between the numerical solution (MODFLOW-NWT) and the analytical solution (14) for $t_0 = 5$ days under instantaneous injection ($\alpha = 0$).

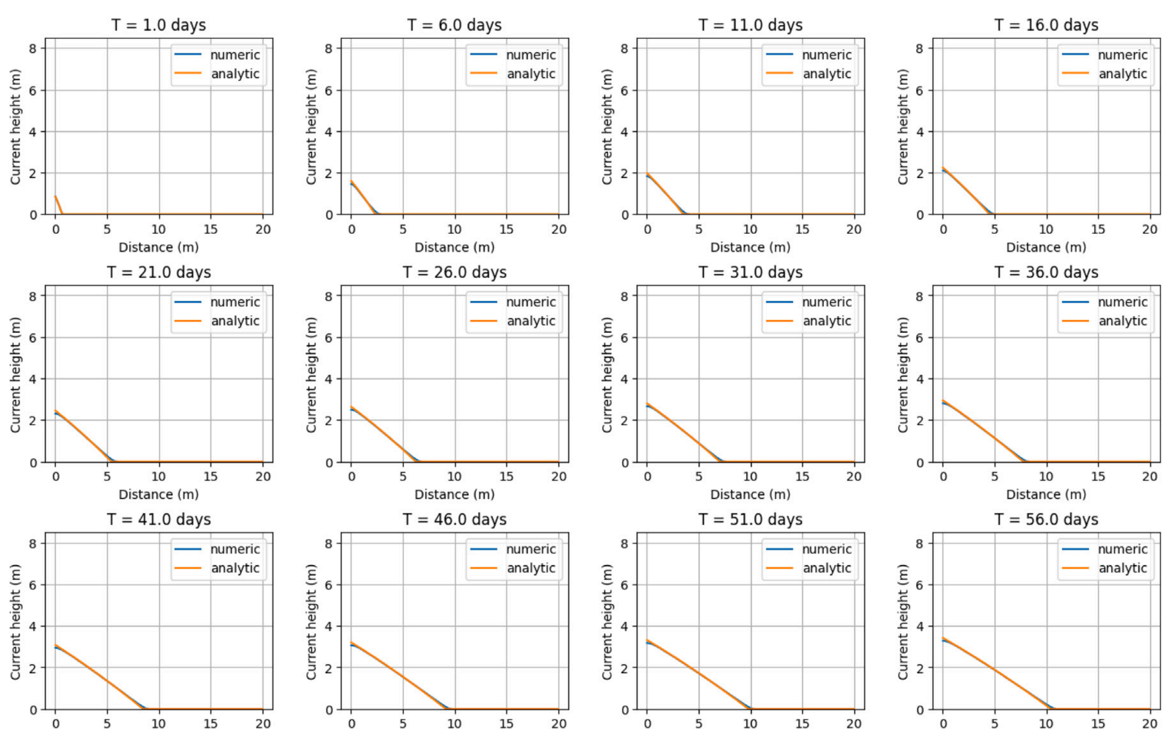

Fig. 6. Comparison between the numerical solution (MODFLOW-NWT) and the analytical solution (17) for $t_0 = 1$ day under constant injection ($\alpha = 1$).

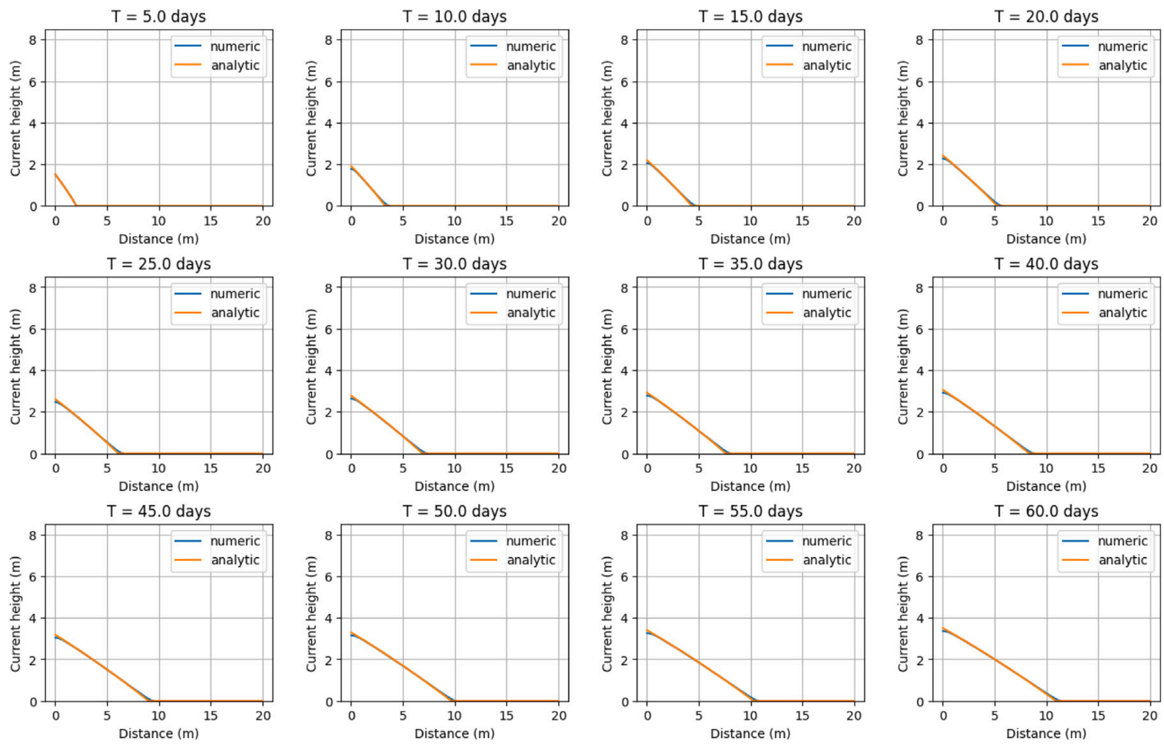

Fig. 7. Comparison between the numerical solution (MODFLOW-NWT) and the analytical solution for $t_0 = 5$ days under constant injection ($\alpha = 1$).

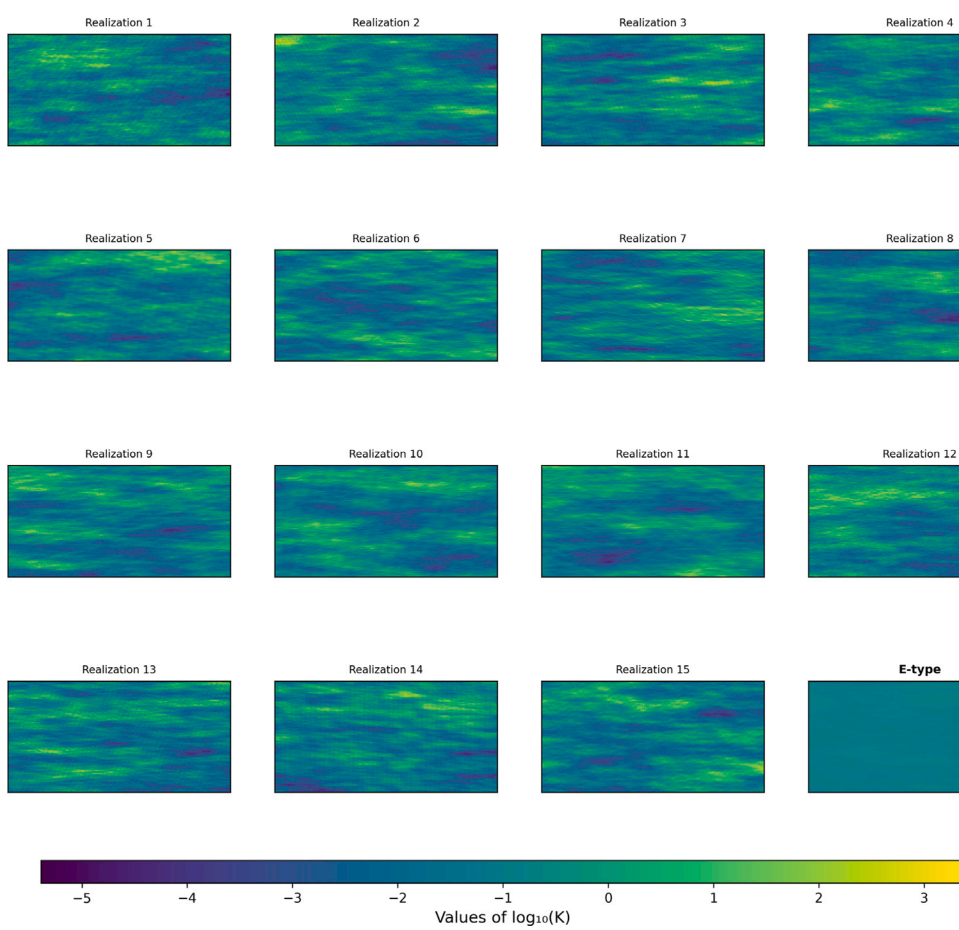

Fig. 8. Realizations drawn from a Gaussian random field with $\log_{10} K$ variance of 1 $(\log_{10} \text{m/day})^2$. Fifteen realizations are shown plus the average of the 100 realizations (E-type). The constant value of the ensemble mean reflects that the realizations are non-conditional.

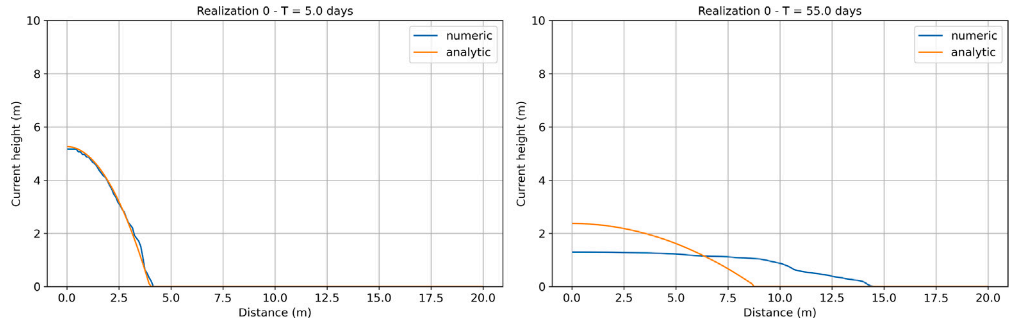

Fig. 9. Initial conditions at $t = 5$ days and current profiles at $t = 55$ days for both the homogeneous field and one of the Gaussian realizations.

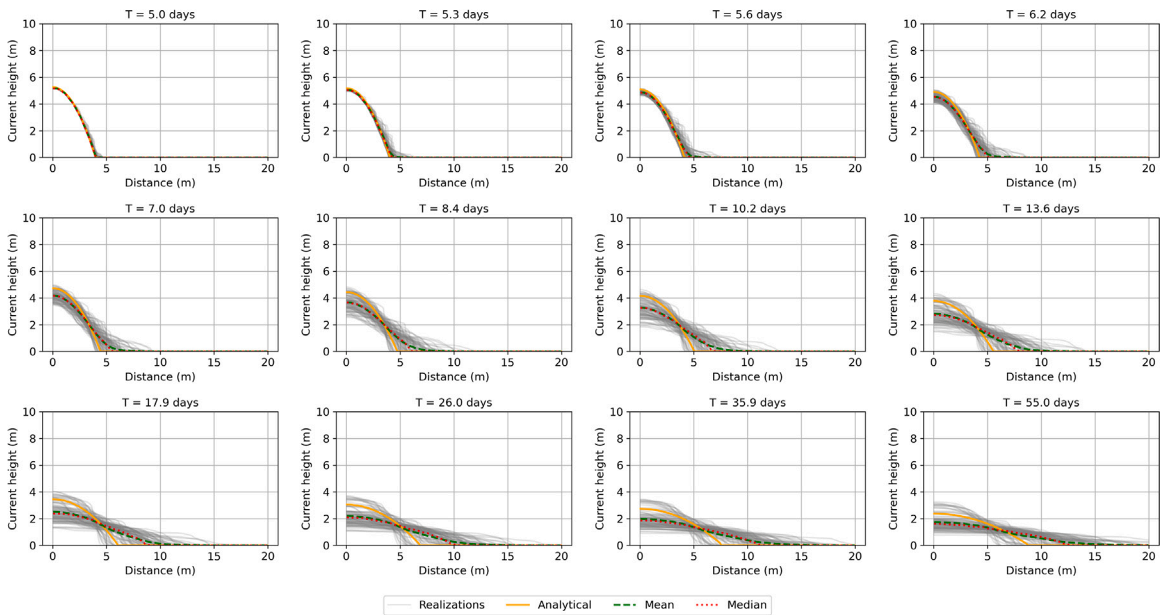

Fig. 10. Temporal evolution of the water table levels for all Gaussian heterogeneity realizations, considering a variance $\sigma^2 = 1.0$ and $\alpha = 0$.

the initial conditions, corresponding to the profile that develops in a homogeneous medium at $t_0 = 5$ days; the right panel displays the current profiles at $t = 55$ days for both the homogeneous case and the selected heterogeneous realization. For the homogeneous case, the analytical solution is shown for a field with $\log_{10} K = -1 \log_{10}$ m/day. A marked difference between the two profiles is evident: the tip of the current advances significantly faster in the heterogeneous field than in the homogeneous one.

Although the latter behavior does not occur in every case, Fig. 10 shows the evolution of the current for all 100 realizations at different times, together with the corresponding profiles in the homogeneous field for $\alpha = 0$ and $\sigma^2 = 1$. Statistics such as the mean and median of the realizations are also computed and shown in the figure. For most heterogeneous realizations, the tip of the current advances more rapidly than in the homogeneous case, although a few realizations exhibit slower propagation. Nonetheless, on average – based on both the mean and median profiles – the current tip travels faster in the heterogeneous fields.

An alternative representation of the impact of heterogeneity is provided in Fig. 11, which shows probability maps indicating the likelihood that the current has reached a given location as a function of the $\log_{10} K$ variance. In all three cases, the current propagates, on average, faster in the heterogeneous realizations than in the homogeneous one having a permeability equal to the average. The median profile – corresponding to the 0.5 isoline – can be interpreted as a "best estimate" of the current position in a heterogeneous medium, while the interval between two extreme isolines, such as the 0.1 and 0.9 curves, provides a measure of the uncertainty associated with this estimate. Besides, both the average advance of the current tip and the associated uncertainty increase as the $\log_{10} K$ variance becomes larger.

4.2. Non-Gaussian heterogeneity

Although the realizations generated using a Gaussian random function are more realistic than either a homogeneous field or a perfectly stratified one, the type of heterogeneity they display may still not adequately reflect natural conditions (Gómez-Hernández and Wen, 1998). Gaussian heterogeneous fields can appear unrealistic for many porous media, as real subsurface formations often display complex spatial structures, resulting from the site-specific depositional processes that produced the geological units.

To reproduce this facies distribution, non-Gaussian heterogeneity fields were generated through unconditional simulations using the EROSIM code (Schorpp et al., 2025), which uses a novel surface-based approach to represent aquifer heterogeneity in sedimentary formations. This method generates complex geological structures by constructing equiprobable surfaces and partitioning the domain into discrete regions, to which values of $\log_{10} K$ are assigned according to a log-normal distribution. The distribution parameters are adjusted so that the mean matches the hydraulic conductivity used in the homogeneous case, while the variance is set to one of the prescribed levels ($\sigma^2 = 0.5; 1.0; 2.0$) ($\log_{10}$ m/day)^2. In our study, the non-Gaussian simulations

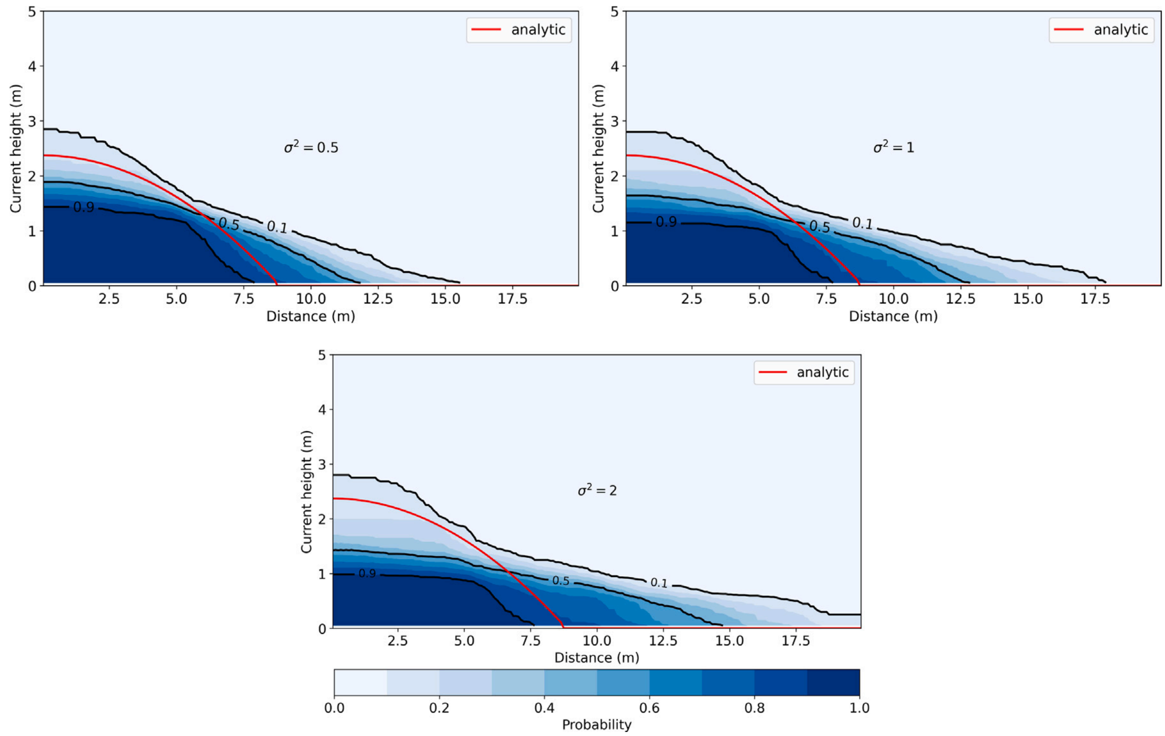

Fig. 11. Probability maps of current arrival at $t = 55$ days for $\alpha = 0$ and the three levels of $\log_{10} K$ variance: from top to bottom, 0.5, 1.0 and 2.0. Darker blue shades indicate a higher probability of arrival. Black curves denote probability isolines, which can be used to define uncertainty intervals, and the red curve represents the current in a homogeneous medium with log-conductivity equal to the mean value of the heterogeneous field.

were generated using the same exponential variogram ($\lambda_h = 4.50$ m and $\lambda_v = 0.67$ m) as that employed for the Gaussian fields, ensuring a consistent spatial correlation structure between both sets of realizations. Actually, in our workflow, the non-Gaussian fields were generated first, and the variogram computed from them was then used to generate the Gaussian realizations.

Fig. 12 shows 15 of the 100 realizations generated by EROSIM, together with their ensemble average. The $\log_{10} K$ mean is -1.0 $\log_{10}$ m/day, the $\log_{10} K$ variance is 1 ($\log_{10}$ m/day)^2, and the variogram is identical to that used to generate the Gaussian realizations. Although the Gaussian and non-Gaussian sets coincide in their first- and second-order moments, a simple visual inspection reveals marked differences between them: the EROSIM realizations exhibit structural patterns that more closely resemble realistic subsurface heterogeneity.

The EROSIM realizations were generated with five facies and 50 structural surfaces. For the simulation of the gravity current migration, the domain geometry, spatial and temporal discretization, and the initial and boundary conditions were kept identical to those used in the Gaussian case.

As in the Gaussian case, the initial conditions were computed from the corresponding analytical solutions for the homogeneous porous medium at $t = 5$ days; the transient flow was then simulated using MODFLOW-NWT. Analogously, statistics such as the mean, median, and E-type model were also obtained, together with temporal evolution curves and saturation probability maps. The boundary conditions and numerical setup remained the same for each combination of α and σ^2. The results were then compared with their Gaussian counterparts.

Fig. 13 depicts probability maps for the case of an instantaneous injection of fluid ($\alpha = 0$) for low (top), medium (middle) and high (bottom) variance levels. The left column shows the profiles for the Gaussian random fields, where an evident stretching of the saturation map occurs as the variance of the spatial variability increases. A similar trend is observed in the right column, corresponding to the non-Gaussian heterogeneous case: as the variance increases, the probability curves become flatter and more dispersed, indicating increasing uncertainty with distance. This behavior is expected, as higher variance increases the likelihood that the current encounters zones of very low or very high permeability. The comparison between the Gaussian (left) and non-Gaussian (right) profiles also reveals that the Gaussian cases exhibit distinct features, including asymmetries and heavier tails in the probability distributions. However, all the scenarios highlight that the homogeneous solution would always predict a slower front compared to the “best estimate” provided by the heterogeneous solver.

Fig. 14 shows the corresponding comparison for the case of a constant fluid release ($\alpha = 1$). Similarly to the $\alpha = 0$ scenario, increasing the variance shifts the contour curves farther downstream, indicating greater uncertainty in the predicted saturation as distance increases. The right column of the figure presents the non-Gaussian case, in which the saturation probabilities differ from those in the Gaussian fields shown in the left column. In particular, the non-Gaussian realizations display smoother transitions and a broader region associated with high saturation probabilities. Finally, we note that the homogeneous solution consistently predicts a taller and slower current compared to the heterogeneous cases.

The impact of small-scale heterogeneity on the GC front position for the different heterogeneous scenarios is graphically summarized in Fig. 15. The plot shows the front position predicted by the 0.5 isoline as the best heterogeneous estimate, along with its confidence interval, described by the 0.1 (upper value) and 0.9 (lower value) isolines, for the three variance levels and for both values of α in the Gaussian and non-Gaussian cases. The plot clearly depicts the increasing uncertainty associated with the front position as the $\log_{10} K$ variance increases. Also evident is the greater variability associated with Gaussian heterogeneity compared to the non-Gaussian one, consistent with the more elongated probability distributions visible in Figs. 13 and 14. When compared to the homogeneous front position, the case of instantaneous injection ($\alpha = 1$) shows a marked discrepancy between the homogeneous value and the heterogeneous prediction, with the homogeneous

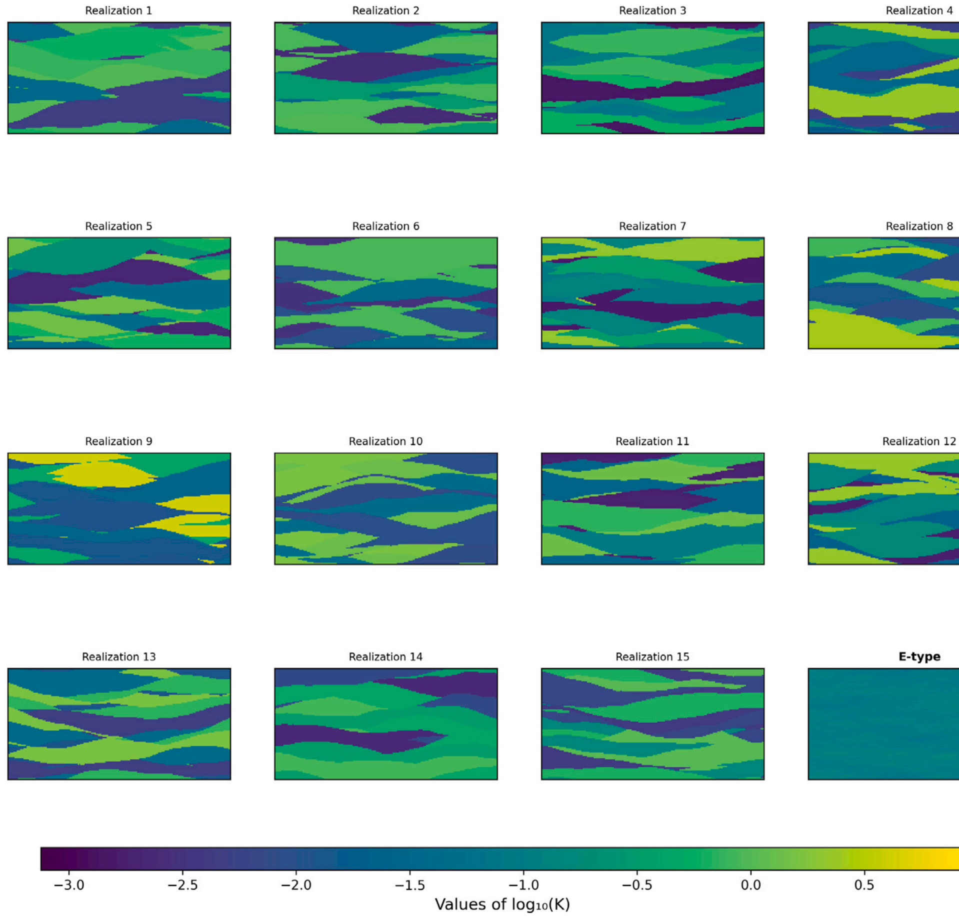

Fig. 12. Sample realizations of a sedimentary porous medium generated using the EROSIM code, together with the ensemble average of the 100 realizations (E-type). The $\log_{10} K$ mean is $-1.0 \log_{10}$ m/day, the $\log_{10} K$ variance is 1 $(\log_{10}$ m/day$)^2$, and the variogram is identical to that used for the Gaussian realizations.

front falling outside the heterogeneous confidence interval in all scenarios. On the other hand, the dam-break release ($\alpha = 0$) shows that the error bar encompasses the homogeneous value, which, however, always underestimates the heterogeneous front position. Note that an arrow in some of the bars indicates that the front position associated with the 0.1 isoline is located at a distance greater than 20 m from the origin, corresponding to the length of the computational domain.

Fig. 16 shows analogous statistics for an additional descriptor of the GC spreading, namely the second central moment of the current S_x^2, computed as

$$S_x^2 = \frac{\int_0^{x_N} (x - x_C)^2 h \, \mathrm{d}x}{\int_0^{x_N} h \, \mathrm{d}x}, \tag{18}$$

where $x_C = \int_0^{x_N} x h \, \mathrm{d}x / \int_0^{x_N} h \, \mathrm{d}x$ is the location of the center of mass of the GC. This quantity is representative of the GC propagation because it quantifies the horizontal spreading of the current around its centroid x_C. When plotted against the three variance levels for both $\alpha = 0$ and $\alpha = 1$, the figure shows that, as the log-conductivity variance increases, the current becomes more stretched in the horizontal direction, reflecting the broader probability regions occupied by the GC in Figs. 13 and 14. Moreover, the non-Gaussian cases shows narrower confidence intervals, i.e., smaller uncertainty, with respect to the Gaussian ones. This is in agreement with the broader tails of the Gaussian probability maps, which result in more elongated profiles in the horizontal direction.

4.3. Convergence analysis

To provide a quantitative illustration of the uncertainty associated with the most extreme heterogeneity, we performed an additional analysis for the non-Gaussian case with $\alpha = 0$ and the highest level of $\log_{10} K$ variance. In this scenario, we first computed the ensemble mean, standard deviation, and classical 95% confidence interval of the front position and the midpoint height ($h_{mid} = h(x_N/2)$) from the $N = 100$ simulated realizations. We then analyzed the convergence of these metrics as a function of the sample size n using a bootstrap resampling scheme (Tibshirani and Efron, 1994). For each n between 5 and N, we generated 500 bootstrap resamples of size n with replacement from the N realizations, computed the mean in each resample, the 95% bootstrap confidence bands and the coefficient of variation. The adoption of a bootstrap approach is motivated by the possibility to approximate the sampling distribution of the two statistics of interest directly from the available ensemble, without imposing additional assumptions on the underlying distribution and while remaining suitable for moderate sample sizes. In addition, we display 20 individual bootstrap trajectories to illustrate the typical variability of the mean estimates as n increases.

Figs. 17 and 18 summarizes the bootstrap convergence of the mean and its coefficient of variation for both the front position and the midpoint height. The main summary statistics for this case are reported in Table 1. Since this case combines non-Gaussian heterogeneity, high variability and $\alpha = 0$ geometry, the resulting uncertainty levels can be regarded as representative of the "worst-case" scenario; thus, in the other heterogeneity cases, uncertainties are expected to be equal or smaller. This analysis shows that both the front position and the midpoint height exhibit a marked decrease in the bootstrap coefficient of variation as the sample size increases, so that the mean estimates become statistically stable once a few dozen realizations are included, even under this worst-case configuration.

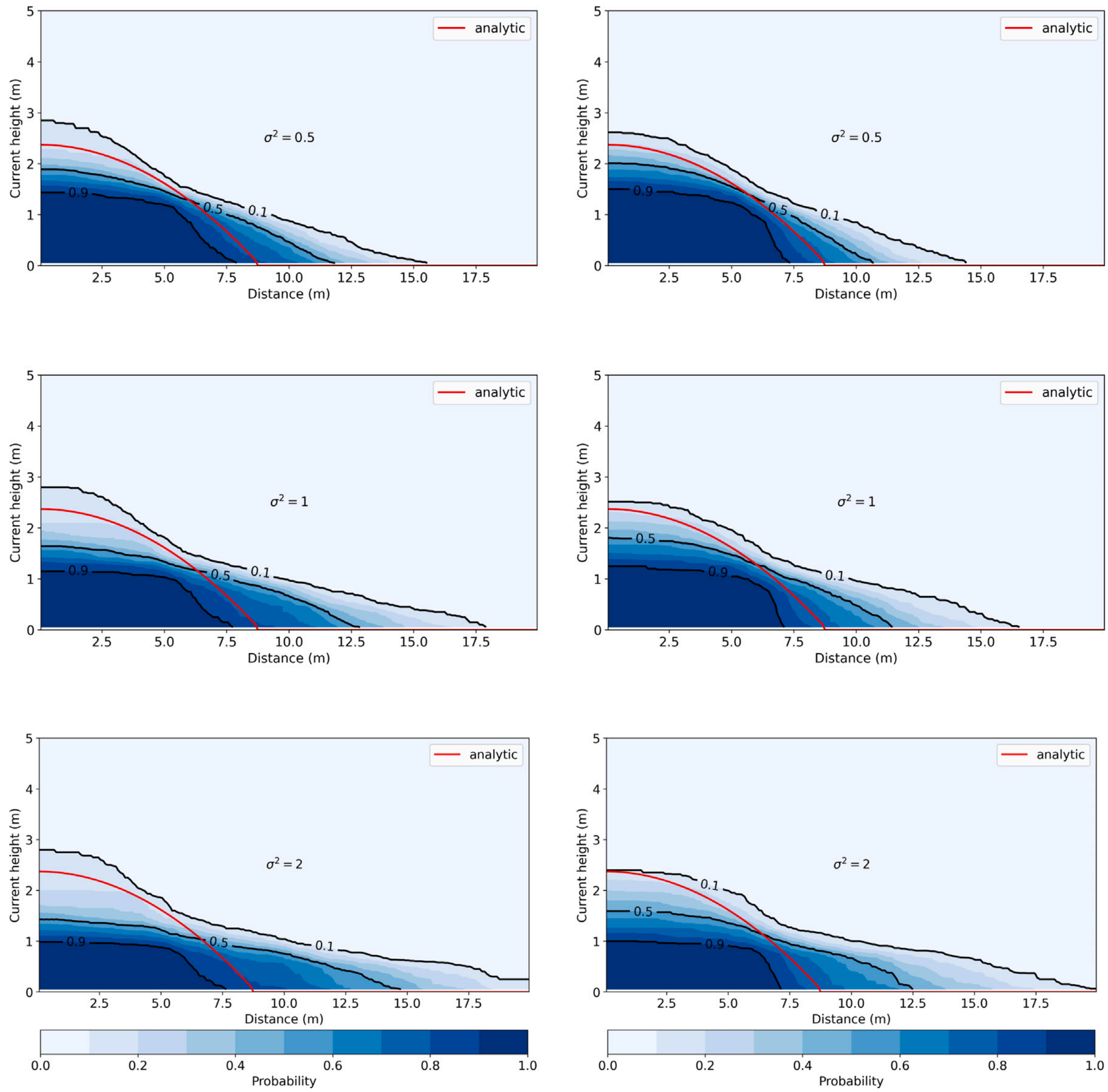

Fig. 13. Comparison of Gaussian and non-Gaussian cases for the saturation probability maps for $\alpha = 0$, 55 days after injection. The left column shows the Gaussian cases, and the right column shows the non-Gaussian cases, for three variance levels of $\log_{10} K$. See Fig. 11 caption for lines and colors description.

Table 1
Summary statistics of the front position and midpoint height for the non-Gaussian case with $\alpha = 0$ and $\log_{10} K$ variance 2.0.

Metric	Front position $\langle x_N \rangle$ (m)	Midpoint height $\langle h_{\mathrm{mid}} \rangle$ (m)
Ensemble mean	12.920	1.041
Standard deviation	4.429	0.388
Standard error of the mean	0.443	0.039
Coefficient of variation (%)	3.428	3.731
95% confidence interval	[12.041, 13.799]	[0.964, 1.118]

4.4. Anisotropy sensitivity analysis

In Sections 4.1 and 4.2, we presented probability maps obtained in a Gaussian and non-Gaussian heterogeneous field for different levels of $log_{10}K$ variance but assuming that both fields are characterized by the same pattern of spatial variability, that is, an exponential variogram with $\lambda_h = 4.50$ m and $\lambda_v = 0.67$ m, which corresponds to an anisotropy ratio $e = \lambda_h/\lambda_v = 6.7$. We now investigate the impact of different anisotropy ratios on the spreading of the gravity current in the heterogeneous porous medium. In particular, we generated 100 Gaussian and 100 non-Gaussian realizations for a high-anisotropy case with $\lambda_h = 8.0$ m and $\lambda_v = 0.67$ m ($e = 11.2$); and a nearly isotropic case with $\lambda_h = 1.33$ m and $\lambda_v = 0.67$ m ($e = 2.0$).

To illustrate the effect of anisotropy on both the conductivity structure and the gravity current, we first present four realizations of the $\log_{10} K$ field for the three anisotropy settings in the Gaussian case (Fig. 19), and then for the non-Gaussian case (Fig. 20), both for $\sigma^2_{\log_{10} K} = 2.0$. The original case $e = 6.7$ we presented in the previous sections is labeled as the “reference” one. The reference fields exhibit moderately elongated structures, whereas the high-anisotropy fields display

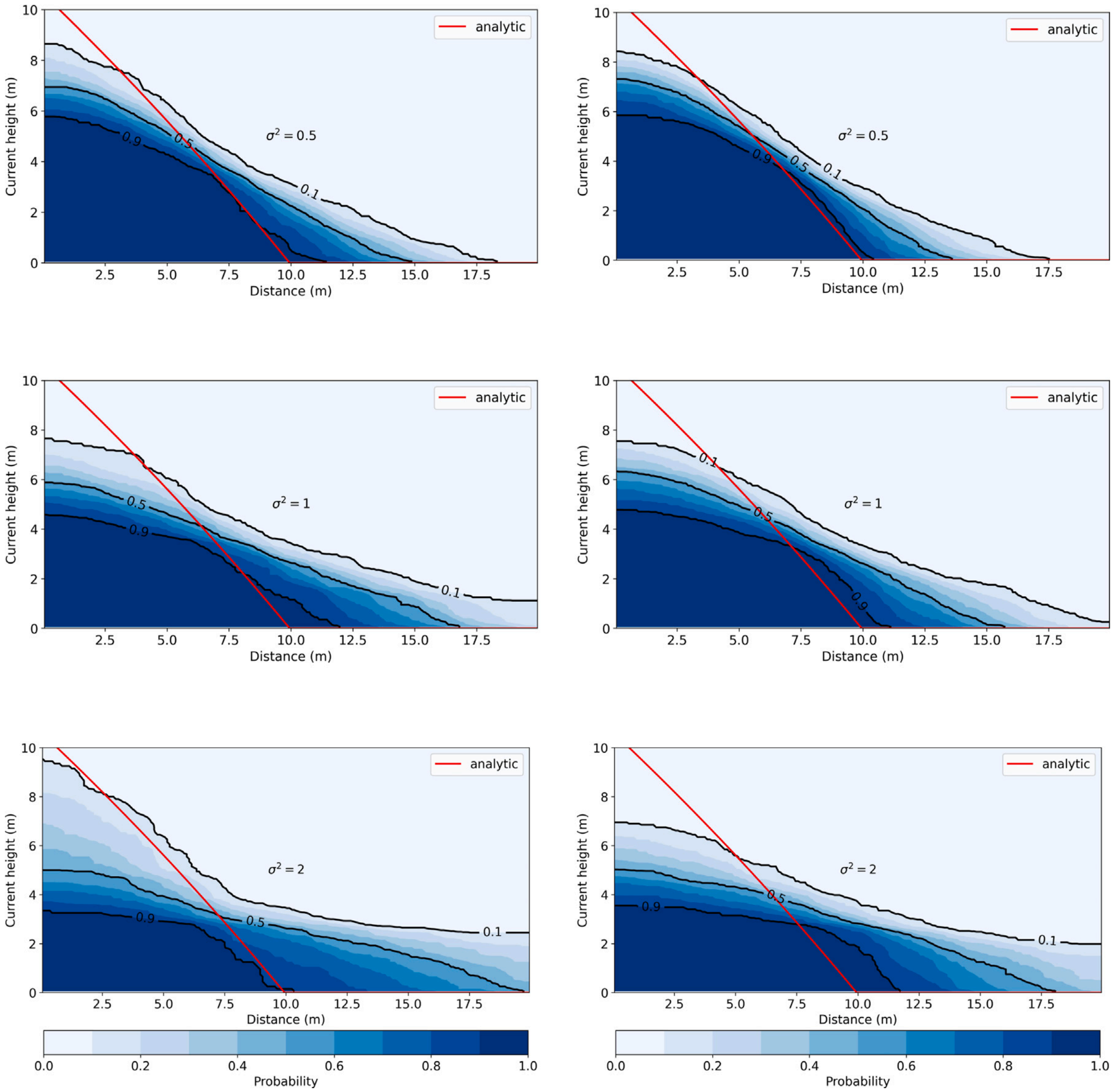

Fig. 14. Comparison of Gaussian and non-Gaussian cases for the saturation probability maps for $\alpha = 1$, 55 days after injection. The left column shows the Gaussian cases, and the right column shows the non-Gaussian cases, for three variance levels of $\log_{10} K$. See Fig. 11 caption for lines and colors description.

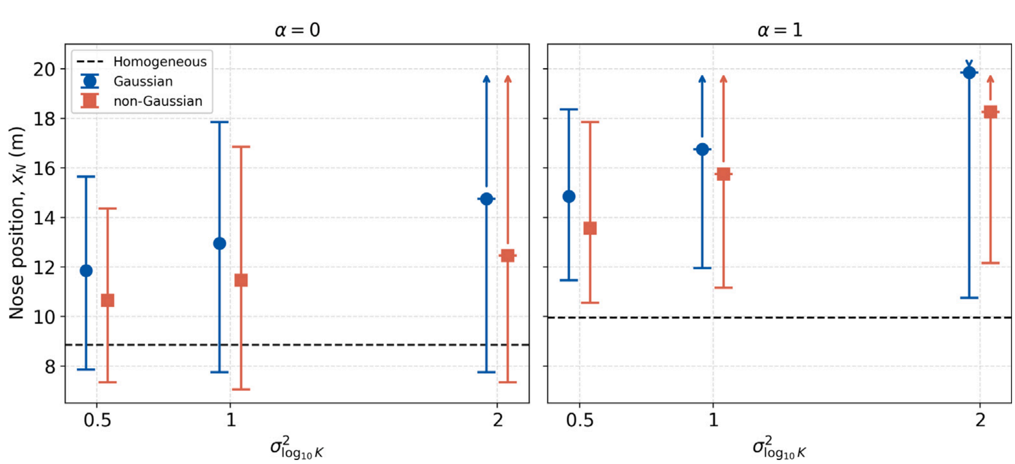

Fig. 15. Heterogeneous versus homogeneous front position for different levels of $\log_{10} K$ variance, 55 days after injection. Blue dots and orange squares denote the front position predicted by the 0.5 isoline, while the upper and lower bounds of the error bars correspond to the 0.1 and 0.9 isolines of the probability map, respectively.

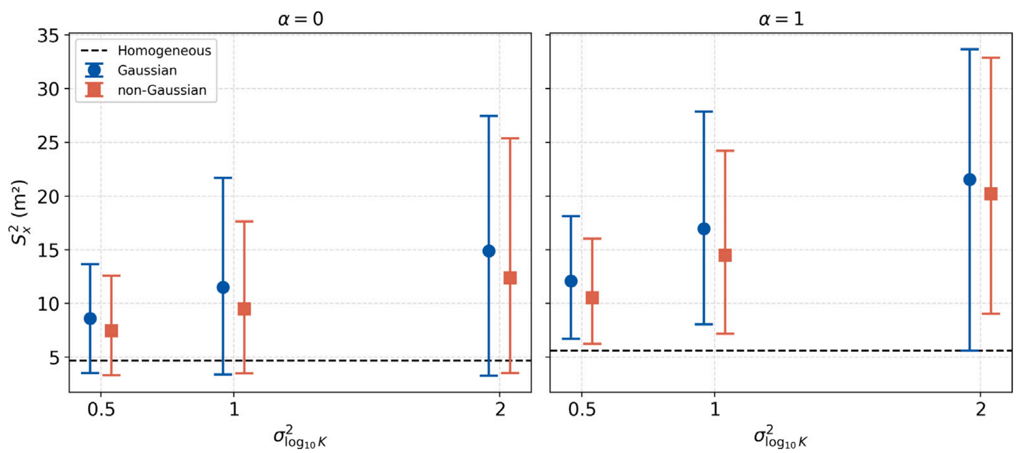

Fig. 16. Heterogeneous versus homogeneous second central moment of the GC for different levels of $\log_{10} K$ variance, 55 days after injection. Blue dots and orange squares denote the estimate based on the 0.5 isoline, while the upper and lower bounds of the error bars correspond to the 0.1 and 0.9 isolines of the probability map, respectively. Horizontal spreading around the centroid is computed using Eq. (18).

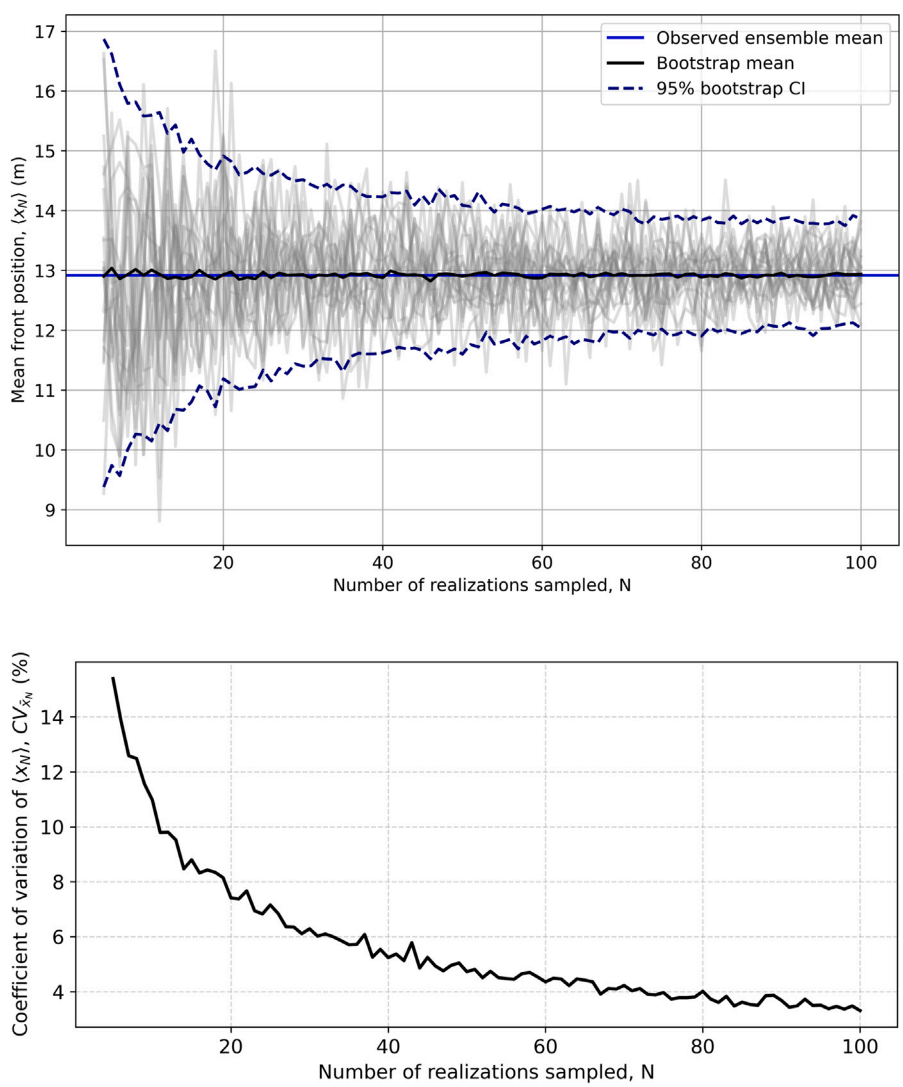

Fig. 17. Bootstrap convergence of the mean and coefficient of variation for the front position in the non-Gaussian case with $\alpha = 0$ and $\log_{10} K$ variance 2.0.

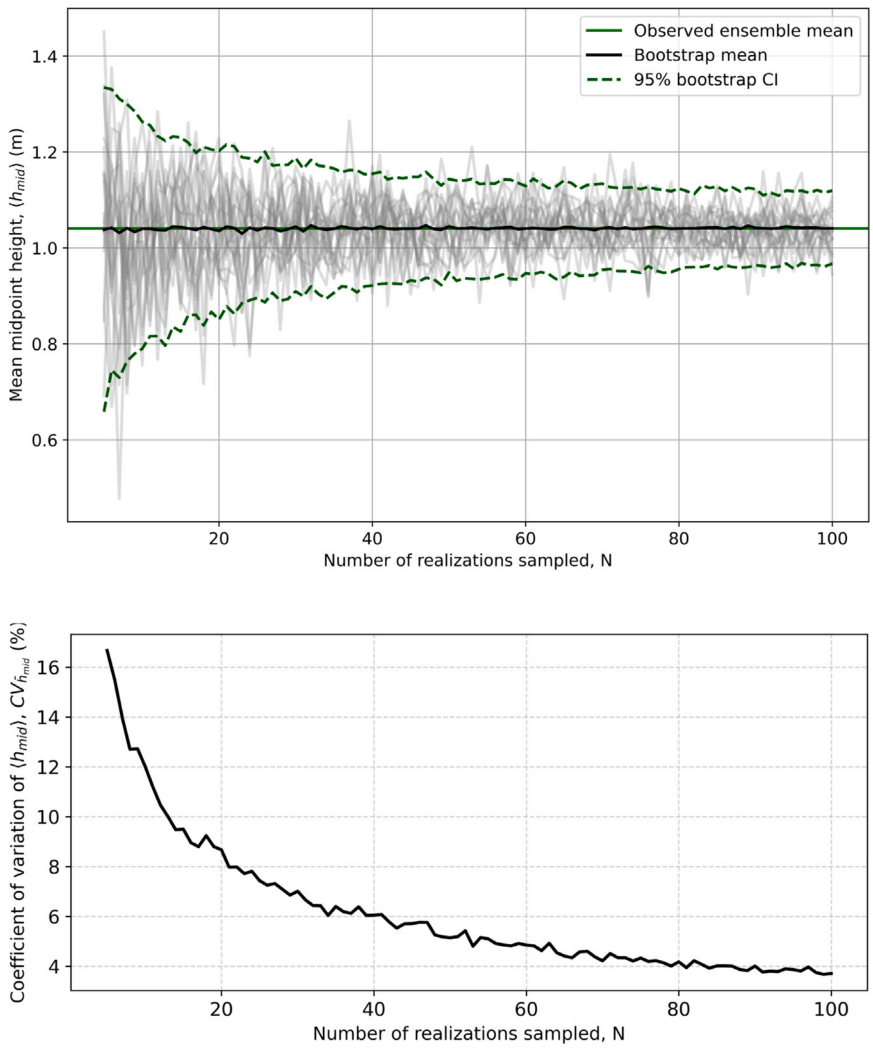

Fig. 18. Bootstrap convergence of the mean and coefficient of variation for the midpoint height in the non-Gaussian case with $\alpha = 0$ and $\log_{10} K$ variance 2.0.

strongly stretched layers aligned with the flow direction. In contrast, the nearly isotropic fields (labeled as “isotropic”) are characterized by more compact and irregular patterns, with reduced spatial continuity in the horizontal direction, reflecting weak anisotropy.

The corresponding probability maps of current arrival at the final time are shown in Fig. 21 for $\alpha = 0$. We note that the case with a $\log_{10} K$ variance of 2.0 and a dam-break release was selected because it represents the “worst-case” scenario, as discussed in Section 4.3. The three anisotropy settings are arranged by rows (reference, high anisotropy, and isotropic, from top to bottom), while Gaussian and non-Gaussian results are presented in the left and right columns, respectively. As expected, in the high-anisotropy scenario the probability map becomes more elongated in the horizontal direction with respect to the reference case for both Gaussian and non-Gaussian heterogeneities, reflecting the impact of anisotropy and the increased uncertainty in the prediction. The opposite behavior is observed in the nearly isotropic case, where the probabilistic region defined by the 0.1 isoline becomes sensitively smaller, and the 0.5 isoline approaches the analytical homogeneous solution. Furthermore, comparison between the left and right columns shows that, while in the reference and high-anisotropy cases the non-Gaussian probability maps are systematically less elongated than the Gaussian ones, this trend is slightly reversed in the nearly isotropic setting, where Gaussian and non-Gaussian maps display more similar shapes.

To further clarify the impact of medium anisotropy on GC spreading, Fig. 22 provides the counterpart of Fig. 16 for varying anisotropy ratio instead of increasing variance. The left panel corresponds to the “worst” case scenario ($\alpha = 0$, variance 2.0), whereas the right panel shows analogous results for the lowest variability scenario, namely $\alpha = 1$ and variance 0.5. The plot clearly depicts the growing uncertainty in the front position associated with increasing anisotropy for a given variance level. Furthermore, as expected, the case of constant injection ($\alpha = 1$) and minimum variance exhibits much lower variability in the nose position than the “worst-case” scenario with $\alpha = 0$ and maximum variance. For both cases, a progressive departure of the heterogeneous best estimate from the front position predicted by the homogeneous analytical solution is evident as anisotropy increases. However, it is noteworthy that, despite the anisotropy ratio nearly doubling from $e = 6.7$ to $e = 11.2$, the best estimate front position does not increase markedly, especially in the non-Gaussian case, whereas the uncertainty associated with the prediction increases substantially.

This analysis also reveals that one of the main outcomes observed across all scenarios – namely, that heterogeneity promotes farther propagation of the current front compared to the homogeneous case – is closely linked to the choice of spatial structures characterized by horizontal correlation lengths larger than the vertical ones. Notably, this configuration is representative of heterogeneity patterns typically found in real sedimentary formations.

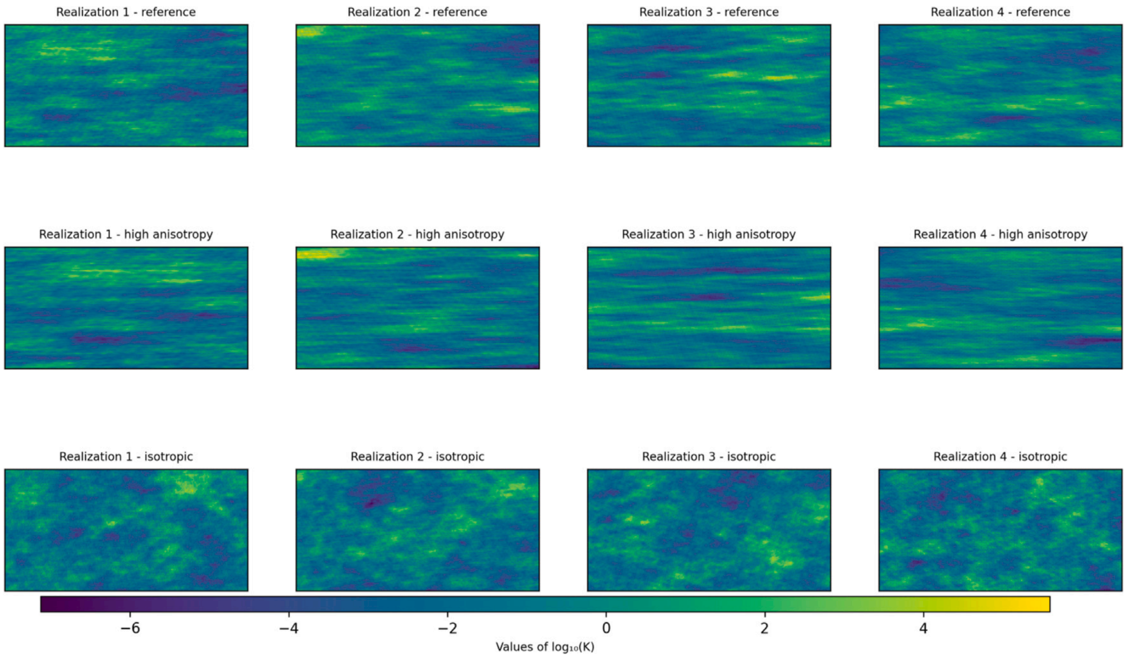

Fig. 19. Sample realizations of the $\log_{10} K$ field for three anisotropy settings in the Gaussian case with $\log_{10} K$ variance 2.0. Top, middle and bottom rows refer to anisotropy ratios equal to $e = 6.7; 11.2; 2.0$, respectively.

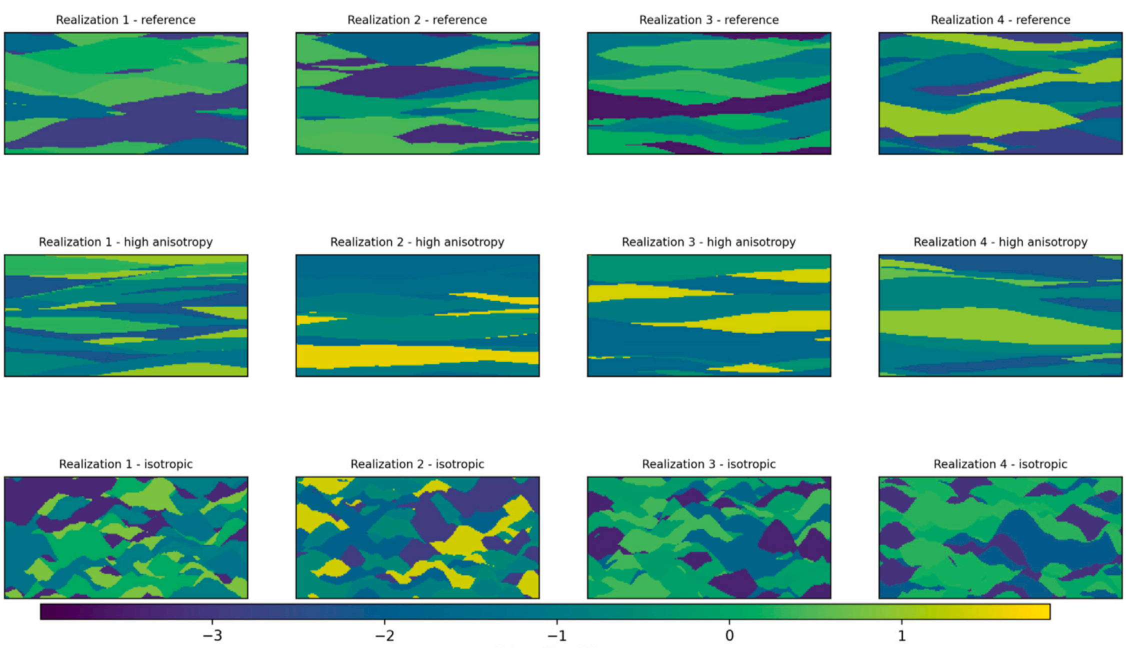

Fig. 20. Sample realizations of the $\log_{10} K$ field for the three anisotropy settings in the non-Gaussian case with $\log_{10} K$ variance 2.0. Top, middle and bottom rows refer to anisotropy ratios equal to $e = 6.7; 11.2; 2.0$, respectively.

5. Discussion and conclusions

As discussed throughout this work, heterogeneity is ubiquitous in natural porous formations, making it essential to account for its effects when modeling gravity currents in realistic applications. In this study, we evaluated the influence of spatial variability in hydraulic conductivity by developing and testing a numerical model capable of incorporating heterogeneous media and assessing their impact on gravity-current propagation.

The MODFLOW-NWT numerical scheme was first validated against the classical similarity solutions derived for a homogeneous porous medium, demonstrating progressively closer agreement between the numerical and analytical profiles as the current advances over time.

We then applied the model to two distinct heterogeneity scenarios. In the first, the spatial variability of hydraulic conductivity was represented as a Gaussian random field, from which 100 independent realizations were generated, yielding 100 corresponding current profiles. This scheme was implemented for three different levels of $\log_{10} K$ variance – low, mild, and high – and for both a finite volume release ($\alpha = 0$) and a constant rate injection ($\alpha = 1$). The temporal evolution of the current revealed that the influence of heterogeneity increases with time: as the current migrates over larger distances,

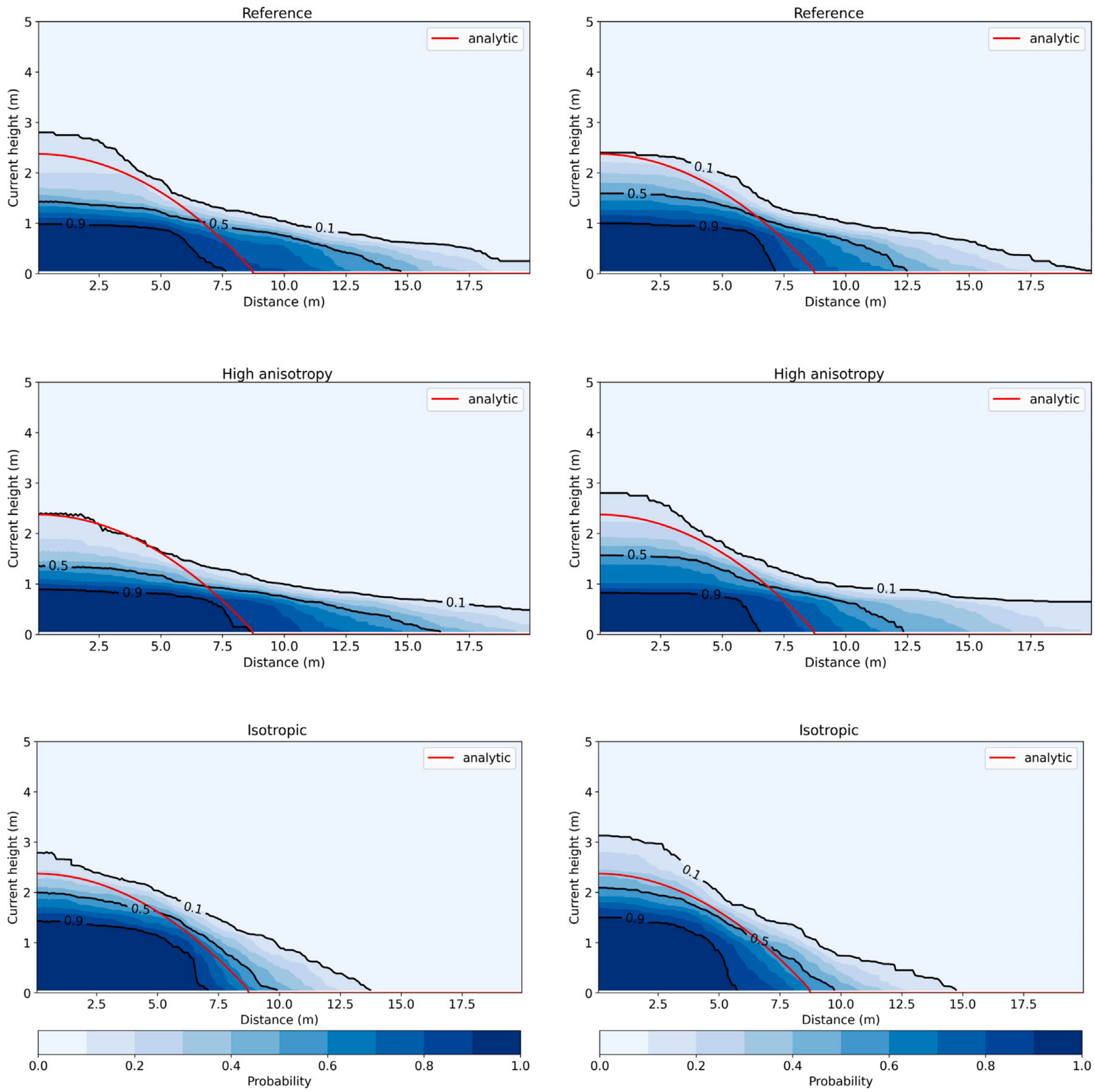

Fig. 21. Probability maps of current arrival at t = 55 days for the three anisotropy settings. The left column shows the Gaussian cases and the right column shows the non-Gaussian cases, both for $\alpha = 0$ and $\log_{10} K$ variance $\sigma^2 = 2.0$. See Fig. 11 caption for lines and colors description.

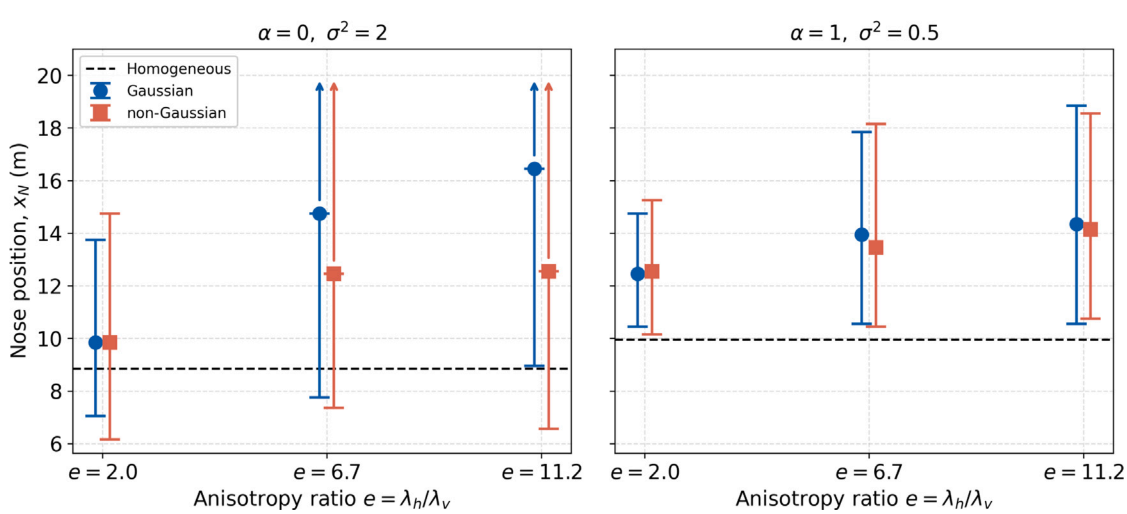

Fig. 22. Heterogeneous versus homogeneous GC front position for different anisotropy ratios, 55 days after injection. Blue dots and orange squares indicate the 0.5 isoline estimate, whereas upper and lower values correspond to the 0.1 and 0.9 isolines of the probability map, respectively.

variations in conductivity cause individual profiles to diverge from the homogeneous reference solution, sometimes advancing more slowly and sometimes more quickly depending on the specific realization. On average, however, we found that heterogeneity tends to accelerate the flow, allowing the current tip to reach farther distances compared with the homogeneous case.

Saturation probability maps were then generated, allowing the definition of probability regions and confidence intervals for the spreading of the current. For instance, the 0.5 isoline can be regarded as a "best estimate" of the current position under heterogeneous conditions. The full set of probability regions also provides a means of quantifying uncertainty in the predictions, with the 0.1 and 0.9 isolines representing bounds on the variability surrounding this "best estimate". By comparing maps corresponding to different variance levels, we showed that greater spatial variability in K leads to higher uncertainty in the saturation forecast, with probability profiles becoming progressively flatter and more elongated as the variance increases.

However, Gaussian heterogeneity does not fully capture the geological complexity typically observed in subsurface porous formations. Real heterogeneity often exhibits distinctive structural patterns that arise from the geological history of the medium. For this reason, in the second scenario we incorporated non-Gaussian heterogeneity into the flow modeling, generated using a rule-based approach that accounts for the presence of geological facies. The results show trends similar to those observed for the Gaussian case: as the variance increases, the saturation maps become more elongated and flattened. However, for the same variance level, the Gaussian probability maps exhibit even more stretching than the non-Gaussian, indicating a higher level of uncertainty in the predicted current position as distance increases.

The comparison with the homogeneous analytical profile highlights the error incurred when heterogeneity is neglected: specifically, the homogeneous analytical solution systematically predicts a slower advancing front than that indicated by the 0.5 isoline of the heterogeneous simulations. This discrepancy is even larger in the Gaussian case for both instantaneous ($\alpha = 0$) and constant ($\alpha = 1$) injection, due to the more stretched probability profiles. Since the non-Gaussian realizations more closely resemble realistic geological heterogeneity, these findings suggest that although the homogeneous solution yields a smaller prediction error in the non-Gaussian case, it still provides a noticeably slower estimate of gravity-current propagation.

To broaden the outcomes of how the spatial structure of the conductivity field influences the GC spreading, we finally evaluated the impact of different anisotropy ratios by generating Gaussian and non-Gaussian realizations for a highly anisotropic case, with an almost doubled horizontal correlation length, and a nearly isotropic case, in which $e = \lambda_h/\lambda_v = 2$ while the reference case has $e = 6.7$. The comparison shows that higher values of the λ_h result in more stretched probability maps, thus increasing the uncertainty of the propagation forecast.

Beyond the specific scenarios considered here, the results highlight a general implication for density-driven flows in heterogeneous porous media. In practical applications, such as groundwater remediation, saline intrusion, brine migration, and geological CO_2 storage, predictions of gravity-current propagation are often used to support engineering decisions and risk assessments. Our findings indicate that neglecting small-scale heterogeneity may lead not only to biased estimates of current migration but also to a substantial underestimation of the uncertainty associated with its future position. This emphasizes the importance of incorporating realistic descriptions of subsurface heterogeneity when forecasting the evolution of density-driven flows in natural formations.

With this work, we demonstrated the impact of different heterogeneity fields on the spreading of a Newtonian gravity current within a porous medium by developing a numerical model capable of accounting for spatial variability in domain properties. We showed how distinct forms of heterogeneity influence gravity-current behavior and quantified the uncertainty that arises in forecasting its evolution over time. Such insights support more accurate predictions of current propagation, which are crucial for relevant applications such as groundwater remediation and understanding CO_2 migration following subsurface injection. However, these problems would require different modeling assumptions, i.e. solving transport and/or multiphase-flow equations, which are not within the scope of this work. Therefore, opportunities remain to further enhance predictive capabilities. Incorporating additional physical complexities – such as capillary forces, fractures, or irregular bottom topography – would provide a more comprehensive representation of real porous media and constitutes an important direction for future work.

CRediT authorship contribution statement

Sepideh Majdabadi Farahani: Writing – original draft, Software, Methodology, Investigation, Data curation, Conceptualization. **Patricio Hernández-Parra:** Writing – original draft, Software, Investigation, Data curation. **Bruno Rossi:** Writing – original draft, Software, Data curation. **Vittorio Di Federico:** Writing – review & editing, Supervision, Project administration, Investigation, Funding acquisition, Conceptualization. **J. Jaime Gómez-Hernández:** Writing – review & editing, Supervision, Software, Project administration, Investigation, Funding acquisition, Conceptualization.

Funding

Sepideh Majdabadi Farahani acknowledges the financial support from Università di Bologna, through the Doctoral Scholarship "Gravity currents in porous media" (PhD@DICAM, Call 2022).

Bruno Rossi acknowledges the financial support from Università di Bologna, through the Doctoral Scholarship "Free-surface flow in heterogeneous porous media" (PhD@DICAM, Call 2025).

Patricio Hernández-Parra acknowledges the financial support from the National Agency for Research and Development (ANID), Chile, through the Doctoral Scholarship "Becas Chile" No. 72230124 (Doctoral Scholarship Abroad, Call 2023).

Vittorio Di Federico acknowledges partial support from Università di Bologna "Ricerca fondamentale Orientata (RFO)" grant 2023.

Declaration of competing interest

The authors declare the following financial interests/personal relationships which may be considered as potential competing interests: Given his role as Associate Editor, Vittorio Di Federico had no involvement in the peer review of this article and had no access to information regarding its peer review. Full responsibility for the editorial process for this article was delegated to another journal editor. If there are other authors, they declare that they have no known competing financial interests or personal relationships that could have appeared to influence the work reported in this paper.

Availability of code

The Python code used for the different simulations can be obtained from the authors.

References

Alamara, H., Blondeau, C., Thibeau, S., Bogdanov, I., 2025. Vertical equilibrium simulation for industrial-scale CO2 storage in heterogeneous aquifers. Sci. Rep. 15 (1), 17115. http://dx.doi.org/10.21203/rs.3.rs-5691633/v1.

Amir, O., Dagan, G., 2002. Uniform steady free-surface flow in heterogeneous porous formations. J. Fluid Mech. 454, 327–343. http://dx.doi.org/10.1017/s002211200100711x.

Anderson, D., McLaughlin, R., Miller, C., 2003. The averaging of gravity currents in porous media. Phys. Fluids 15 (10), 2810–2829. http://dx.doi.org/10.1063/1.1600733.

Barenblatt, G., 1996. Scaling, Self-Similarity, and Intermediate Asymptotics: Dimensional Analysis and Intermediate Asymptotics. (14), Cambridge University Press, http://dx.doi.org/10.1017/CBO9781107050242.

Bear, J., 1972. Dynamics of Fluids in Porous Media. Courier Corporation, http://dx.doi.org/10.1017/S0022112073210662.

Benham, G., Bickle, M., Neufeld, J., 2021. Two-phase gravity currents in layered porous media. J. Fluid Mech. 922, A7. http://dx.doi.org/10.1017/jfm.2021.523.

Ciriello, V., Di Federico, V., Archetti, R., Longo, S., 2013. Effect of variable permeability on the propagation of thin gravity currents in porous media. Int. J. Non-Linear Mech. 57, 168–175. http://dx.doi.org/10.1016/j.ijnonlinmec.2013.07.003.

Crevillén-García, D., Leung, P., Rodchanarowan, A., Shah, A., 2019. Uncertainty quantification for flow and transport in highly heterogeneous porous media based on simultaneous stochastic model dimensionality reduction. Transp. Porous Media 126 (1), 79–95. http://dx.doi.org/10.1007/s11242-018-1114-2.

Di Federico, V., Archetti, R., Longo, S., 2012. Similarity solutions for spreading of a two-dimensional non-Newtonian gravity current in a porous layer. J. Non-Newton. Fluid Mech. 177, 46–53. http://dx.doi.org/10.1016/j.jnnfm.2012.04.003.

Dussan, E., Auzerais, F., 1993. Buoyancy-induced flow in porous media generated near a drilled oil well. Part 1. The accumulation of filtrate at a horizontal impermeable boundary. J. Fluid Mech. 254, http://dx.doi.org/10.1017/s0022112093002137.

Farcas, A., Woods, A., 2015. Buoyancy-driven dispersion in a layered porous rock. J. Fluid Mech. 767, 226–239. http://dx.doi.org/10.1017/jfm.2014.744.

Flicos, E., Neufeld, J., 2025. Response of a gravity current in a porous medium to a perturbation of the permeability field. J. Fluid Mech. 1024, A29. http://dx.doi.org/10.1017/jfm.2025.10868.

Franzetti, S., Guadagnini, A., 1996. Probabilistic estimation of well catchments in heterogeneous aquifers. J. Hydrol. 174 (1–2), 149–171. http://dx.doi.org/10.1016/0022-1694(95)02750-5.

Goda, T., Sato, K., 2011. Gravity currents of carbon dioxide with residual gas trapping in a two-layered porous medium. J. Fluid Mech. 673, 60–79. http://dx.doi.org/10.1017/s0022112010006178.

Gómez-Hernández, J.J., Wen, X.-H., 1998. To be or not to be multiGaussian: A reflection in stochastic hydrogeology. Adv. Water Resour. 21 (1), 47–61. http://dx.doi.org/10.1016/s0309-1708(96)00031-0.

Guo, Z., Fogg, G.E., Brusseau, M.L., LaBolle, E.M., Lopez, J., 2019. Modeling groundwater contaminant transport in the presence of large heterogeneity: a case study comparing MT3D and RWhet. Hydrogeol. J. 27 (4), 1363–1371. http://dx.doi.org/10.1007/s10040-019-01938-9.

Hewitt, D., Peng, G., Lister, J.R., 2020. Buoyancy-driven plumes in a layered porous medium. J. Fluid Mech. 883, A37. http://dx.doi.org/10.1017/jfm.2019.888.

Huppert, H., 1982. Flow and instability of a viscous current down a slope. Nature 300 (5891), 427–429. http://dx.doi.org/10.1038/300427a0.

Huppert, H., Neufeld, J., Strandkvist, C., 2013. The competition between gravity and flow focusing in two-layered porous media. J. Fluid Mech. 720, 5–14. http://dx.doi.org/10.1017/jfm.2012.623.

Huppert, H., Woods, A., 1995. Gravity-driven flows in porous layers. J. Fluid Mech. 292, 55–69. http://dx.doi.org/10.1017/s0022112095001431.

Krevor, S., Pini, R., Li, B., Benson, S., 2011. Capillary heterogeneity trapping of CO2 in a sandstone rock at reservoir conditions. Geophys. Res. Lett. 38 (15), http://dx.doi.org/10.1029/2011gl048239.

Lennon, G., Bowers, D., Nunes, R., Scott, B., Ali, M., Boyle, J., Wenju, C., Herzfeld, M., Johansson, G., Nield, S., et al., 1987. Gravity currents and the release of salt from an inverse estuary. Nature 327 (6124), 695–697. http://dx.doi.org/10.1038/327695a0.

Longo, S., Ciriello, V., Chiapponi, L., Di Federico, V., 2015. Combined effect of rheology and confining boundaries on spreading of gravity currents in porous media. Adv. Water Resour. 79, 140–152. http://dx.doi.org/10.1016/j.advwatres.2015.02.016.

Lyle, S., Huppert, H., Hallworth, M., Bickle, M., Chadwick, A., 2005. Axisymmetric gravity currents in a porous medium. J. Fluid Mech. 543, 293–302. http://dx.doi.org/10.1017/s0022112005006713.

Maggi, M., Adduce, C., Lane-Serff, G., 2023. Gravity currents interacting with slopes and overhangs. Adv. Water Resour. 171, 104339. http://dx.doi.org/10.1016/j.advwatres.2022.104339.

Mathunjwa, J., Hogg, A., 2007. Freely draining gravity currents in porous media: dipole self-similar solutions with and without capillary retention. European J. Appl. Math. 18 (3), 337–362. http://dx.doi.org/10.1017/s0956792507006985.

Maxwell, R.M., Carle, S.F., Tompson, A.F., 2008. Contamination, risk, and heterogeneity: on the effectiveness of aquifer remediation. Environ. Geol. 54 (8), 1771–1786. http://dx.doi.org/10.1007/s00254-007-0955-8.

Michael, H.A., Khan, M.R., 2016. Impacts of physical and chemical aquifer heterogeneity on basin-scale solute transport: Vulnerability of deep groundwater to arsenic contamination in Bangladesh. Adv. Water Resour. 98, 147–158. http://dx.doi.org/10.1016/j.advwatres.2016.10.010.

Michigan State University, 2005. Real World Heterogeneity. IGW Visualization Library, URL: https://www.egr.msu.edu/igw/DL/RWH/RWH17.htm.

Mo, S., Zhu, Y., Zabaras, N., Shi, X., Wu, J., 2019. Deep convolutional encoder-decoder networks for uncertainty quantification of dynamic multiphase flow in heterogeneous media. Water Resour. Res. 55 (1), 703–728. http://dx.doi.org/10.1029/2018wr023528.

Neufeld, J., Huppert, H., 2009. Modelling carbon dioxide sequestration in layered strata. J. Fluid Mech. 625, 353–370. http://dx.doi.org/10.1017/s0022112008005703.

Pegler, S., Huppert, H., Neufeld, J., 2013. Topographic controls on gravity currents in porous media. J. Fluid Mech. 734, 317–337. http://dx.doi.org/10.1017/jfm.2013.466.

Sahu, C., Neufeld, J., 2020. Dispersive entrainment into gravity currents in porous media. J. Fluid Mech. 886, A5. http://dx.doi.org/10.1103/yc98-f1fx.

Sahu, C., Neufeld, J., 2023. Experimental insights into gravity-driven flows and mixing in layered porous media. J. Fluid Mech. 956, A27. http://dx.doi.org/10.1017/jfm.2022.1082.

Savoy, H., Kalbacher, T., Dietrich, P., Rubin, Y., 2017. Geological heterogeneity: Goal-oriented simplification of structure and characterization needs. Adv. Water Resour. 109, 1–13. http://dx.doi.org/10.1016/j.advwatres.2017.08.017.

Schneider, L., di Chiara Roupert, R., Schäfer, G., Helluy, P., 2015. Highly gravity-driven flow of a NAPL in water-saturated porous media using the discontinuous Galerkin finite-element method with a generalised Godunov scheme. Comput. Geosci. 19, 855–876. http://dx.doi.org/10.1007/s10596-015-9494-7.

Schorpp, L., Straubhaar, J., Renard, P., 2025. A novel surface-based approach to represent aquifer heterogeneity in sedimentary formations. Water Resour. Res. 61 (2), http://dx.doi.org/10.22541/essoar.170612218.80961459/v1.

Tartakovsky, D.M., Winter, C., 2001. Dynamics of free surfaces in random porous media. SIAM J. Appl. Math. 61 (6), 1857–1876.

Tibshirani, R.J., Efron, B., 1994. An introduction to the bootstrap. Monogr. Statist. Appl. Probab. 57 (1), 1–436. http://dx.doi.org/10.1201/9780429246593.

Tosco, T., Papini, M.P., Viggi, C.C., Sethi, R., 2014. Nanoscale zerovalent iron particles for groundwater remediation: a review. J. Clean. Prod. 77, 10–21. http://dx.doi.org/10.1016/j.jclepro.2013.12.026.

Woods, A., 1998. Vaporizing gravity currents in a superheated porous medium. J. Fluid Mech. 377, 151–168. http://dx.doi.org/10.1017/s0022112098003012.

Woods, A., 1999. Liquid and vapor flow in superheated rock. Annu. Rev. Fluid Mech. 31 (1), 171–199. http://dx.doi.org/10.1146/annurev.fluid.31.1.171.

Woods, A., Mason, R., 2000. The dynamics of two-layer gravity-driven flows in permeable rock. J. Fluid Mech. 421, 83–114. http://dx.doi.org/10.1017/s0022112000001567.

Zheng, Z., Soh, B., Huppert, H., Stone, H., 2013. Fluid drainage from the edge of a porous reservoir. J. Fluid Mech. 718, 558–568. http://dx.doi.org/10.1017/jfm.2012.630.